CHALMERS
UNIVERSITY OF TECHNOLOGY

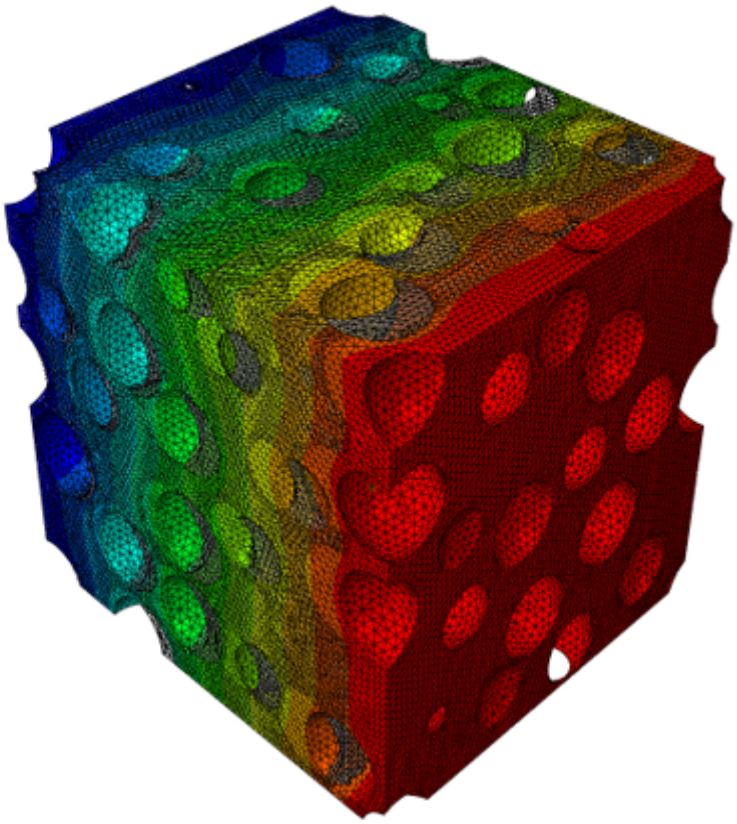

Mechanical Material Modelling and Characterisation of Li-ion Battery

Master's thesis report in Materials Engineering

Amit Chetry

DEPARTMENT OF INDUSTRIAL AND MATERIALS SCIENCE
CHALMERS UNIVERSITY OF TECHNOLOGY
Gothenburg, Sweden 2024
www.chalmers.se

MASTER'S THESIS REPORT 2024

Mechanical Material Modelling and Characterisation of Li-ion Battery

Amit Chetry

CHALMERS
UNIVERSITY OF TECHNOLOGY

Department of Industrial and Materials Science
Division of Material and Computational Mechanics
CHALMERS UNIVERSITY OF TECHNOLOGY
Gothenburg, Sweden 2024

Mechanical Material Modelling and Characterisation of Li-ion Battery.

AMIT CHETRY

© AMIT CHETRY, 2024.

Supervisor: David Carlstedt, Simon Vikström, and Peter Gustavsson, Volvo Cars
Examiner: Leif Asp, Industrial and Materials Science

Master's thesis report 2024
Department of Industrial and Materials Science
Chalmers University of Technology
SE-412 96 Gothenburg
Sweden
Telephone +46 31 772 1000

Cover: Displacement-driven simulation of porous separator implementing Dirichlet boundary conditions.

Printed by Chalmers Reproservice
Gothenburg, Sweden 2024

Mechanical Material Modelling and Characterisation of Li-ion Battery.

AMIT CHETRY
Department of Industrial and Materials Science
Chalmers University of Technology

Abstract

The increasing demand for sustainable energy solutions has propelled the development of electric vehicles (EVs) and the need for high-performance, reliable batteries. This study focuses on the material modelling of lithium-ion battery cells to enhance their safety and performance under mechanical loads. Initially, a linear elastic model was employed as a preliminary approach to develop the modelling strategy. Subsequently, hyperelastic modelling was explored but revealed a stiffer response than observed in real-world conditions, making it unreliable for capturing the complex behaviour of the battery's electrode materials. Consequently, a crushable foam material model was implemented, providing a more accurate representation of the electrodes' response to mechanical loads. Through a multi-scale homogenization process, this study effectively links the mechanical response at the microstructural level to the overall behaviour of the battery cell, providing insights into stress and strain distributions within individual battery components. This approach paves the way for improved modelling strategies in the future that can predict failure scenarios, such as short circuits, thereby contributing to the design of safer and more reliable EV batteries. Limitations of the study include its focus on quasi-static loading conditions and the exclusion of electrochemical and thermal effects, suggesting areas for future research.

Keywords: Electric vehicles (EVs), Lithium-ion batteries, Finite Element Method (FEM), Hyperelastic model, and Crushable foam model.

Acknowledgements

I want to show my gratitude towards my supervisors David Carlstedt, Simon Vikström and Peter Gustavsson for their immense support and guidance during the entire thesis. Their knowledge and experience helped me to sharpen my understanding of FEM. I also want to thank the entire FEM structure team of Volvo Cars. They always guided me and helped me when I approached them with doubts.

Furthermore, I want to thank my examiner Leif Asp for his support. His feedback and insights into the problems faced were of immense help. I also want to thank Prof. Fredrik Larsson for his support and input during the monthly thesis meetings.

My family and friends are of great source of positive energy for me, without them I would not be the person I am today. Finally, I want to say that Mom, Dad, and sister, I Love You, thank you for everything.

Amit Chetry, Gothenburg, May 2024

List of Acronyms

Below is the list of acronyms that have been used throughout this thesis listed in alphabetical order:

CB	Carbon black
EVs	Electric Vehicles
FEM	Finite Element Method
LFP	Lithium Iron Phosphate
Li-ion	Lithium-ion
MD	Material Direction
NCA	Lithium Nickel Cobalt Aluminium Oxide
NMC	Lithium Nickel Manganese Cobalt Oxide
PE	Polyethylene
PP	Polypropylene
RVE	Representative Volume Element
SOC	State of Charge
SOH	State of Health
TD	Transverse Direction

Contents

List of Figures

List of Tables

1

Introduction

The global increase in population and their demands have pushed the energy sector to rely on fossil fuels predominantly. One sector which has been significantly affected by this is the automotive sector. To move away from this dependency, electric vehicles (EVs) are being developed. EVs produce relatively very low pollution compared to internal combustion engine vehicles, therefore contributing towards sustainable transportation. To increase the efficiency and performance of EVs, different strategies to design high-energy density batteries and to extract the best performance out of them are being developed. However, what comes with this advancement is the increased risk of potential battery failure scenarios during a crash.

Electric vehicles are exposed to different types of mechanical forces during operation. Battery systems designed to sustain mechanical loads associated with such conditions are being developed to ensure safe and reliable battery structures while minimising the potential risk of short circuits or malfunction.

To ensure the safety and reliability of the EV battery packs, battery cells are tested under different conditions e.g., indentation, tension, compression, residual stress due to swelling etc. To capture the mechanical response of the batteries under such conditions, it is important to understand the interplay between the microstructure and the constituent properties. In this study, constituent-level modelling strategies to capture the cell's response to quasi-static loading have been developed.

1.1 Background

In EVs, the stack of cells is presented in the form of modules and battery packs. The deformation of the single cell is highly influenced by its neighbouring cells. The batteries form a cushion foundation for each other during accidental loads in the event of a crash [1]. Therefore it is very important to understand the behaviour of the battery during such events. The main parts of the battery cell are electrodes, separators, and current collectors (as seen in Figure 1.1).

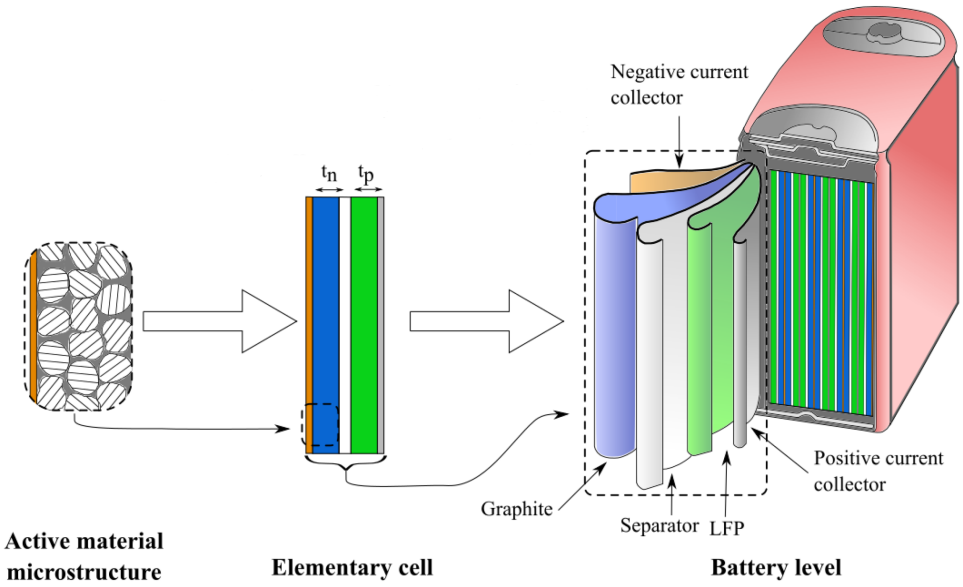

Figure 1.1: Illustration of the micro-structure of the active particles and different components of a prismatic graphite-lithium ion phosphate (LFP) battery cell and its stacking in the form of jellyroll, which is a multilayer stacking of electrodes, current collectors and separators, adapted from [2].

1.1.1 Material properties of battery components

The material properties of the battery components differ from each other. The current collectors have an influential role in the in-plane tension of the cathode and anode layers, compared to the adhesion of the coating's particles to the metallic layer or the cohesion between those particles [1]. The metallic current collectors exhibit ductility, therefore plastic flow is seen in tensile tests [1], shown in Figure 1.2.

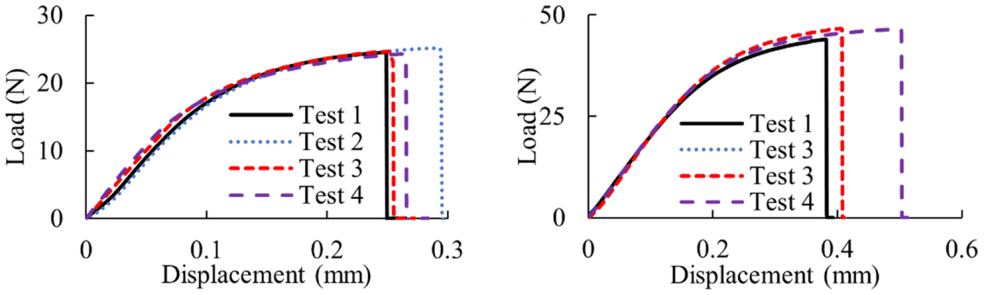

Figure 1.2: Material response of the anode (left) and cathode (right) under tension, showing the difference in failure strength and displacement because of different current collectors (copper for anode and aluminium for cathode) attached, adapted from [1].

The role of the metallic current collector is not significant in axial compression tests compared with tension. The polymer binder Polyvinylidene fluoride (PVDF) used to bind the electrode particles (lithium iron phosphate (LFP) for the cathode and

graphite for the anode) is highly porous. Therefore, at the beginning of a compression test, the distance between the active particles is reduced while pores are compressed. The final failure occurs when the porous polymer-electrolyte system is fully compacted and cracks are formed [1].

The separator, which is usually made of Polypropylene (PP) or polyethylene (PE), however, typically shows in-plane anisotropy in the material direction (MD) versus the transverse direction (TD) (see Figure 1.3) due to their fabrication process [1]. Therefore, it is important to understand the material properties of the constituents and individual layers to develop a reliable material model or failure criteria.

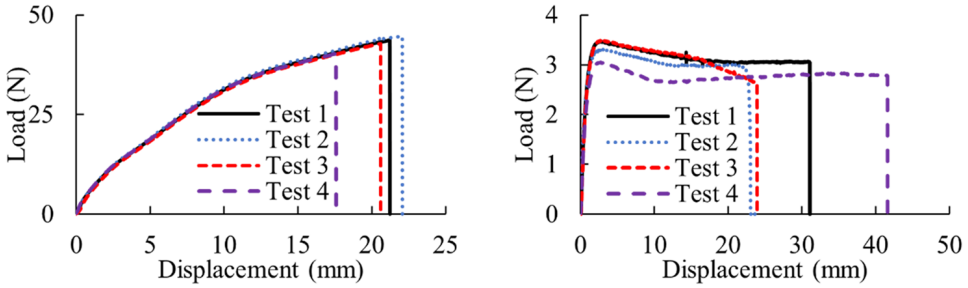

Figure 1.3: Material response of the separator in manufacturing direction (left) and transverse direction (right), showing anisotropy because of the porous structure, adapted from [1].

1.1.2 Mechanical material modelling of battery cell

The most widely implemented modelling strategies for predicting the mechanical response of the jellyroll are the crushable foam and honeycomb material models. For example, Greve et al. considered the jellyroll as isotropic by considering the deformation of the electrodes together with the separator as an integrated and continuous system. However, the influence of frictional slip between the layers and the influence of the potential foil separation (gaping) is neglected [3]. Xu et al. developed a modelling strategy to continue this work where they implemented the flow rule for the uniaxial compression and an anisotropic model for the three-point bending condition [4]. However, they assumed the material to be transversely isotropic to simplify the model.

Further, Gupta et al. modelled the cell considering the stacking of active layers, current collectors, and the separators as a multi-layer composite and implemented mechanical homogenisation using the 3D laminate theory [5]. They considered the swelling effect as a factor in their model. This approach is very pivotal and promising, however, what is lacking in this model is the constituent level consideration. The authors have assumed the material properties of the individual layers. The possibility of measuring and predicting these properties is considered one of the most important gaps in the current research in this field.

In this study, FEM models are prepared based on Representative Volume Elements (RVEs) of the microstructure of the active layers and the separator as illustrated in Figure 1.4. The RVE study at the nanoscale, where the individual constituents are modelled, is used to extract homogenised material properties of different layers to the RVE of the stack. Similarly, the homogenised properties of the stack will be implemented as an input to the final jellyroll model. This will make the model more robust and reliable. Therefore, addressing the previously mentioned gap.

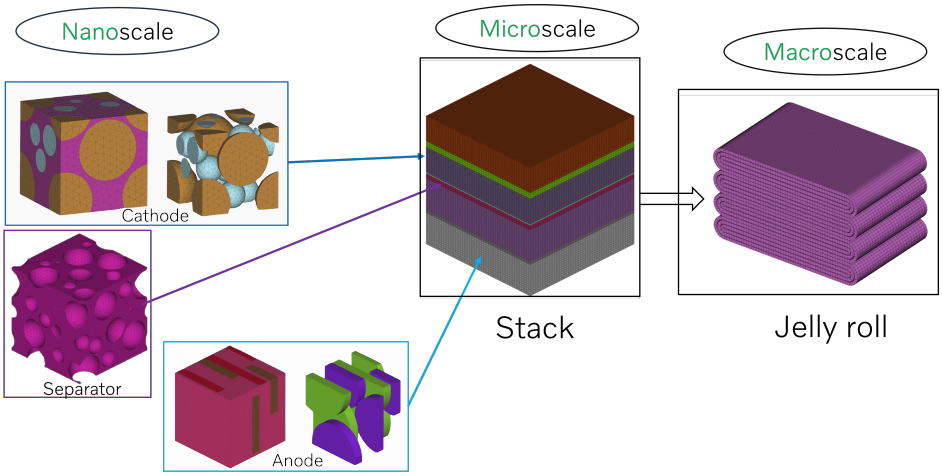

Figure 1.4: Model description of the implementation of an RVE of the microstructure of the active material and its further implementation in the RVE of the stack. Finally, the homogenised material properties will be used to model the response of the jellyroll.

1.2 Aims and approach

The thesis' aims are to develop a material model to capture the mechanical response of batteries at the cell level and its validation under mechanical loading conditions. The thesis' utmost priority is to increase the safety and reliability of EV cars by developing more reliable modelling design tools. The scope of this thesis includes the following:

1. Homogenisation of the material properties from the nanoscale to the macroscale.
2. Literature survey to find the required material data for the electrodes, separator, and current collectors.
3. Characterise the material properties by upscaling the effective properties of different components at various scales.
4. Develop a multiscale modelling strategy of the battery as a material independent of form factor, chemistry or design.
5. Define test plans for future model validation and verification.

1.3 Limitations

The developed material model is based on the homogenised response of the battery cell obtained from the characterization and discretization of the constituents within the jellyroll. The study is limited to the quasi-static response of single Li-ion batteries. This thesis does not study the module level and the pack level mechanical response. The study of other factors such as crash tests and short circuit prediction is also outside this project's scope.

Furthermore, the operation of Li-ion batteries themselves involves a lot of complexity, ranging from nanoscale to macroscale as well as different phenomena like electrical, thermal, and mechanical couplings. The multi-physics involved are not considered. The liquid electrolyte is also not explicitly modelled and the charge-discharge cycles are not evaluated in terms of the voltage-current response. However, these topics can be the potential future scope of the project.

2
Theory

2.1 Battery

The battery is one of the most efficient energy-storing devices to date. A battery stores and delivers energy by the release and movement of Li-ions and electrons between the cathode and the anode via the electrolyte and an external circuit, respectively. In other words, batteries convert electrical energy into chemical energy during charging and chemical energy into electrical energy during discharge. While used in the automotive application, the electrical energy is converted into mechanical energy which is then utilised to propel the vehicle ahead. Different technologies are developed to monitor the charge-discharge cycle of the batteries and maintain high operation efficiency and performance. For example, the battery pack used by Volvo Cars in the EX90 Twin Motor model has a total capacity of 111 kWh with 204 cells and a total voltage of 400 V. The cathode material used in these battery cells is Lithium nickel manganese cobalt oxide (NMC) [6].

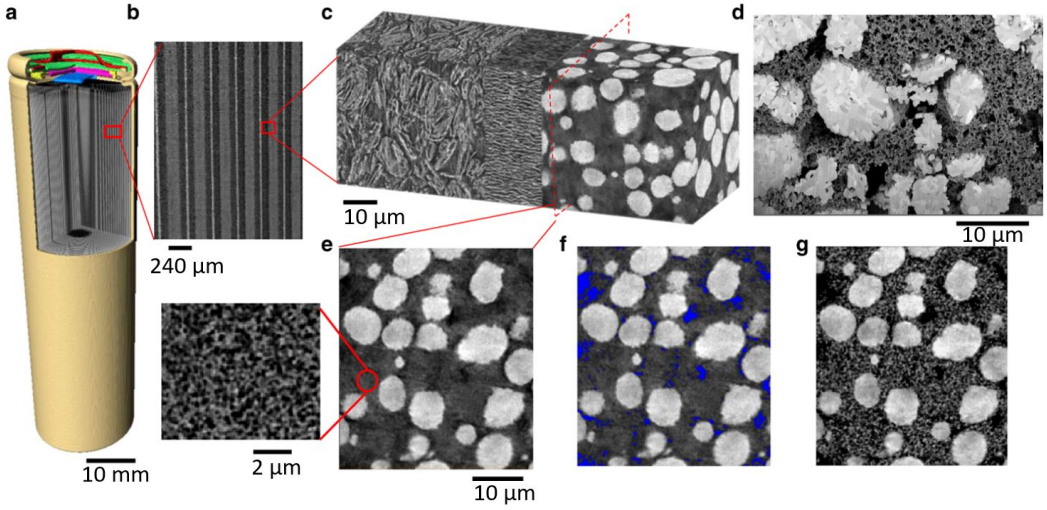

Figure 2.1: Figure demonstrating the complexity in modelling of a battery because of the involved length scales, presence of nanopores in the binder with liquid electrolyte, irregular microstructure of the active material particles etc. Adapted from [7]

Figure 2.1(a) shows the configuration of a cylindrical battery with a diameter of 20 mm which has NMC as the cathode and graphite as the anode material. Figure

2.1(b) shows the stacking sequence of the separator and the electrodes attached to the metallic current collectors, each stack is in the order of 240 μm. Figure 2.1(c) shows (from left to right) the graphite anode, polyolefin separator and NMC cathode. It also shows how the particles of NMC are distributed inside the binder as well as the flakes-like micro-structure of the graphite, separated by a highly porous separator. Figure 2.1(d)-(g) show the porous nature of the polymer binder-conductive additive network, where the pores of this porous structure are filled with liquid electrolytes. This demonstrates the complexities involved when attempting to predict the response of this multi-phase material. Therefore, careful consideration of this multi-phase system for material modelling is of great importance to capture the real response of the battery as material undergoing deformation due to mechanical loading.

2.1.1 Electrode material

The chemistry of the battery controls its overall performance and efficiency. Therefore, it is important to choose the active materials wisely. Different cathode materials currently available include; e.g., NMC, Lithium nickel cobalt aluminium oxide (NCA), and Lithium iron phosphate (LFP) [8]. The nature and properties of the anode material are crucial to the overall performance of a battery. The battery's capacity and efficiency depend significantly on the intrinsic characteristics of the anode material as well as its morphology. Therefore, the structural design is often more critical than the material itself. Numerous high-performance anode materials are being explored for the next generation of lithium-ion batteries (LIBs), including alloy materials, conversion-type transition metal compounds, silicon-based compounds, and carbon-based compounds [9].

2.1.2 Current collector

The electrode layer is attached to the current collector to enable the transfer of electrons. Based on the type of electrode layers, the current collector materials vary. Copper (Cu) foil is typically attached to the anode and aluminium (Al) foil is attached to the cathode. These two metal foils take an active role when the battery is under mechanical load, in particular when these layers are under tension. Since these metal foils are normal metals, they can be considered isotropic and homogeneous at the studied length scale. Hence, following the material model of Hooke's law till the elastic limit and non-linear plasticity beyond the yield point can be used. In other words, these materials can be considered as a system of a spring and a slider in series in the form of physical description of the material response [10].

2.1.3 Separator

The separator plays a vital role in maintaining ion transfer between the anode and the cathode while preventing any contact between them which would lead to a short circuit. Their nano-porous structure can be seen in Figure 2.2. In other words, the separator prevents rapid energy drainage by not allowing the free electron

to pass through, therefore avoiding short circuits. The most common separator materials are Polypropylene (PP) and Polyethylene (PE). They are manufactured using wet or dry processes, whereas the wet process is mainly for the PE. Eventually, a ceramic composite is applied to the separator with an engraving roller to meet the requirements of a Li-ion battery [11].

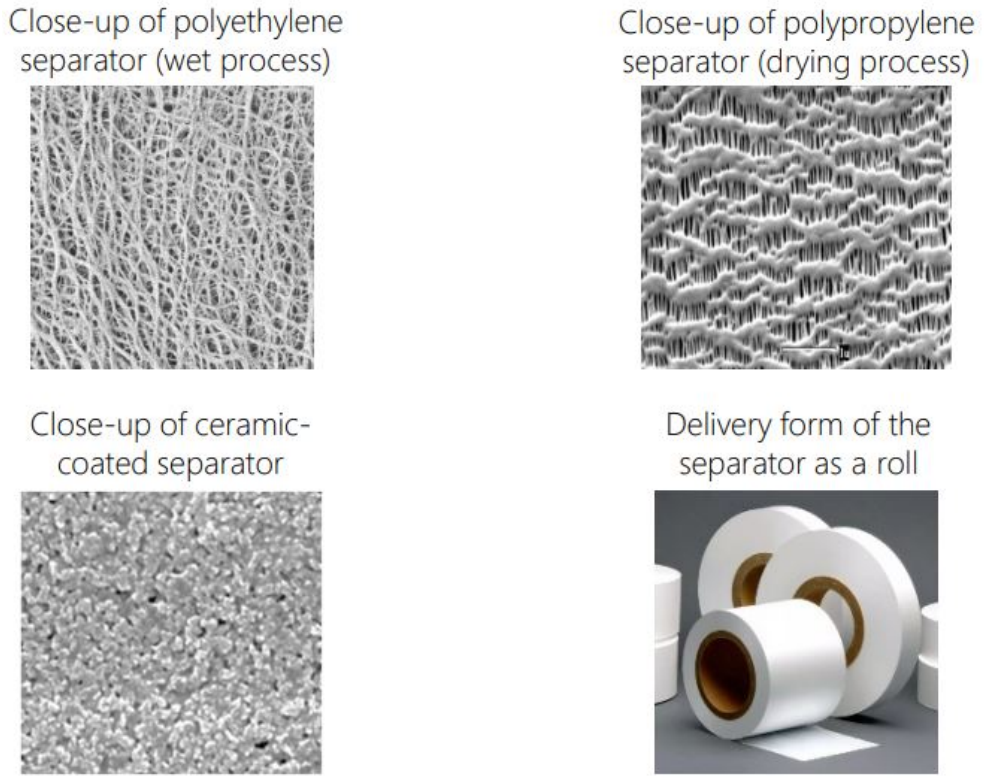

Figure 2.2: Figure demonstrating the different microstructure of the separator based on manufacturing processes and types, reprint from [11].

2.1.4 Casing

Cell casing is another important component of a battery. It provides the housing of the cell and serves as the first barrier to the jellyroll from the oxygen-rich, humid environment. Furthermore, it serves as the first barrier when it comes to mechanical abuse. Therefore, it is also possible that, under certain mechanical loads, the cell case takes all the load and no force reaches the jellyroll, keeping it safe and away from a potential short circuit. The most commonly used material for the cell casing is deep-drawn aluminium. A deep-drawn aluminium is highly anisotropic, because of varying thickness in the direction of drawing done to induce residual stress which makes the material work hardened.

2.2 Material's response to loads

The laws of attraction and repulsion of atoms, when they are separated from an equilibrium position, have a great influence on the material's response to loads. If the material is isotropic it shows the same behaviour in all three directions. When a material is strained, the equilibrium position of these atoms is altered or changed, which results in the material experiencing stress. These stresses, when significant, lead to the failure of the material. Therefore, it is important to understand the material's response to different loads.

2.2.1 Linear elastic response

A material can show linear elastic or non-linear elastic response when deformed depending on the microstructure or the composition of the material. The relationship between stress (σ) and strain (ϵ) is one of the most significant aspects of understanding a structural material and its characteristics. The relationship is given by Hooke's law which can be represented as:

$$\sigma_{ij} = C_{ijkl}\epsilon_{kl} \tag{2.1}$$

Equation 2.1 is the Hooke's law in three dimensions (3D). The 3D stiffness tensor C_{ijkl} is a fourth-order tensor with 81 components. For anisotropic materials only 21 components are independent, the remaining 60 components can be written in terms of the other 21. Since the stress and strain tensors are symmetric, i.e, $\sigma_{ij} = \sigma_{ji}$ and $\epsilon_{kl} = \epsilon_{lk}$, it follows that $C_{ijkl} = C_{jikl} = C_{ijlk} = C_{jilk}$, which effectively reduces the number of independent components to 36 [12]. The 36 independent components can be written as a 6X6 matrix as seen in Equation 2.2.

$$\begin{bmatrix}\sigma_1\\ \sigma_2\\ \sigma_3\\ \sigma_4\\ \sigma_5\\ \sigma_6\end{bmatrix} = \begin{bmatrix}C_{11} & C_{12} & C_{13} & C_{14} & C_{15} & C_{16}\\ C_{21} & C_{22} & C_{23} & C_{24} & C_{25} & C_{26}\\ C_{31} & C_{32} & C_{33} & C_{34} & C_{35} & C_{36}\\ C_{41} & C_{42} & C_{43} & C_{44} & C_{45} & C_{46}\\ C_{51} & C_{52} & C_{53} & C_{54} & C_{55} & C_{56}\\ C_{61} & C_{62} & C_{63} & C_{64} & C_{65} & C_{66}\end{bmatrix}\begin{bmatrix}\epsilon_1\\ \epsilon_2\\ \epsilon_3\\ \gamma_4\\ \gamma_5\\ \gamma_6\end{bmatrix} \tag{2.2}$$

2.2.1.1 Orthotropic material

An orthotropic material has three planes of symmetry that coincide with the coordinate planes. When there are two orthogonal planes of symmetry there always exists a third orthogonal plane of symmetry, therefore, for such material only 9 independent components are required. Since the material has symmetry about the 1-3 plane, this means that $C_{i6} = C_{6i} = 0$, $i \neq 6$. In this case, 3D Hooke's law reduces

as shown in Equation 2.3.

$$\begin{bmatrix}\sigma_1\\ \sigma_2\\ \sigma_3\\ \sigma_4\\ \sigma_5\\ \sigma_6\end{bmatrix} = \begin{bmatrix}C_{11} & C_{12} & C_{13} & 0 & 0 & 0\\ C_{12} & C_{22} & C_{23} & 0 & 0 & 0\\ C_{13} & C_{23} & C_{33} & 0 & 0 & 0\\ 0 & 0 & 0 & C_{44} & 0 & 0\\ 0 & 0 & 0 & 0 & C_{55} & 0\\ 0 & 0 & 0 & 0 & 0 & C_{66}\end{bmatrix} \begin{bmatrix}\epsilon_1\\ \epsilon_2\\ \epsilon_3\\ \gamma_4\\ \gamma_5\\ \gamma_6\end{bmatrix} \tag{2.3}$$

2.2.1.2 Transversely isotropic material

A transversely isotropic material has one axis of symmetry, it is described by five independent constants. Hooke's law is reduced to Equation 2.4, where $C_{22} = C_{33}$ and $C_{55} = C_{66}$

$$\begin{bmatrix}\sigma_1\\ \sigma_2\\ \sigma_3\\ \sigma_4\\ \sigma_5\\ \sigma_6\end{bmatrix} = \begin{bmatrix}C_{11} & C_{12} & C_{13} & 0 & 0 & 0\\ C_{12} & C_{22} & C_{23} & 0 & 0 & 0\\ C_{13} & C_{23} & C_{22} & 0 & 0 & 0\\ 0 & 0 & 0 & (C_{22}-C_{23})/2 & 0 & 0\\ 0 & 0 & 0 & 0 & C_{66} & 0\\ 0 & 0 & 0 & 0 & 0 & C_{66}\end{bmatrix} \begin{bmatrix}\epsilon_1\\ \epsilon_2\\ \epsilon_3\\ \gamma_4\\ \gamma_5\\ \gamma_6\end{bmatrix} \tag{2.4}$$

The longitudinal and transverse Young's moduli E_1 and E_2, the longitudinal and transverse Poisson's ratios υ_{12} and υ_{23} and the longitudinal shear modulus G_{12}, can be expressed as the equations below [12]:

$$E_1 = C_{11} - 2C_{12}^2/(C_{22} + C_{23}) \tag{2.5}$$

$$\upsilon_{12} = C_{12}/(C_{22} + C_{23}) \tag{2.6}$$

$$E_2 = [C_{11}(C_{22} + C_{23}) - 2C_{12}^2](C_{22} - C_{23})/(C_{11}C_{22} - C_{12}^2) \tag{2.7}$$

$$\upsilon_{23} = [C_{11}C_{23} - C_{12}^2]/(C_{11}C_{22} - C_{12}^2) \tag{2.8}$$

$$G_{12} = C_{66} \tag{2.9}$$

$$G_{23} = C_{44} = \frac{1}{2}(C_{22} - C_{23}) = \frac{E_2}{2(1 + \upsilon_{23})} \tag{2.10}$$

2.2.2 Elasto-plastic response

Linear elastic-plastic materials exhibit yield points, this yield point is very significant. The material is in an elastic region before this point and once it is reached the material starts to glide, this region is called the plastic region. In other words, the material goes under permanent deformation. These material characteristics are mainly shown by metals. In metals, the plasticity phenomena are mainly governed by dislocation movement. These dislocations start to glide in their favourable slip planes inside the material's microstructure. During this plasticity, the materials also

exhibit strain hardening. Strain hardening can be linear and non-linear based on the material. This strain hardening is mainly because of the dislocation pile-up. When dislocations begin to move, the dislocation density increases. The accumulation of dislocations restricts their movement along the slip plane.

The expression for the free energy also known as Helmholtz free energy for isotropic hardening can be written as Equation 2.11 [10].

$$\psi = \frac{1}{2}E(\epsilon - \epsilon^p)^2 + \frac{1}{2}Hk^2 \tag{2.11}$$

where $\epsilon^e = \epsilon - \epsilon^p$ is the elastic strain of the Hookean spring with a modulus of elasticity E and H is the hardening stiffness. The constitutive equation for the stress can be written as

$$\sigma = \frac{\partial \psi}{\partial \epsilon} = E(\epsilon - \epsilon^p) \tag{2.12}$$

and for the dissipative stress, that is conjugated to ϵ^p, the constitutive equation can be written as

$$\sigma^p = -\frac{\partial \psi}{\partial \epsilon^p} = E(\epsilon - \epsilon^p) \equiv \sigma \tag{2.13}$$

where the dissipative stress K, associated with k, can be written as

$$K = -\frac{\partial \psi}{\partial k} = -Hk \tag{2.14}$$

The yield criterion is $\psi = 0$, where ψ is chosen as

$$\psi(\sigma) = |\sigma| - (\sigma_y + k) \tag{2.15}$$

where k is the micro hardening stress due to isotropic hardening; which is frequently denoted as the drag stress [10].

2.2.3 Hyperelastic response

A material for which the constitutive behaviour is only a function of the current state of deformation is known as simple material. A simple material without memory is called simple elastic material. Under these conditions, stress at particle $\boldsymbol{X}$ is a function of the current deformation gradient $\boldsymbol{F}$ associated with the particle. Since the deformation gradient tensor $\boldsymbol{F}$ is a work conjugate of the first Piola-Kirchoff stress tensor $\boldsymbol{P}$ [13], the elasticity can be expressed as:

$$\boldsymbol{P} = \boldsymbol{P}(\boldsymbol{F}(\boldsymbol{X}), \boldsymbol{X}) \tag{2.16}$$

Where the direct dependency on $\boldsymbol{X}$ allows for the possible inhomogeneity of the material.

In special cases when the work done by the stresses during a deformation process depends only on the initial state at time t_0 and the final configuration at time t, the behaviour of the material is said to be path independent and the material is termed as hyperelastic or green elastic material [13]. Since, $\boldsymbol{P}$ is work conjugate

with the rate of deformation gradient $\dot{\boldsymbol{F}}$, as a consequence of the path-independent behaviour, a stored strain energy function or elastic potential Ψ per unit deformed volume can be established as the work done by the stresses from the initial to the current position as:

$$\Psi(\boldsymbol{F}(\boldsymbol{X}), \boldsymbol{X}) = \int_{t_0}^{t} \boldsymbol{P}(\boldsymbol{F}(\boldsymbol{X}), \boldsymbol{X}) : \dot{\boldsymbol{F}}\, dt; \qquad \dot{\Psi} = \boldsymbol{P} : \dot{\boldsymbol{F}} \tag{2.17}$$

From experiments, it is possible to construct the function of $\Psi(\boldsymbol{F}, \boldsymbol{X})$ which defines a given material, then the rate of change of the potential can be alternatively expressed as:

$$\dot{\Psi} = \sum_{i,J=1}^{3} \frac{\partial \Psi}{\partial F_{iJ}} \dot{F}_{iJ} \tag{2.18}$$

Comparing Equation 2.17 with 2.18, the components of two-point tensor $\boldsymbol{P}$ are revealed:

$$P_{iJ} = \frac{\partial \Psi}{\partial F_{iJ}} \tag{2.19}$$

For notational convenience, this expression is rewritten in a more compact form:

$$\boldsymbol{P}(\boldsymbol{F}(\boldsymbol{X}), \boldsymbol{X}) = \frac{\partial \Psi(\boldsymbol{F}(\boldsymbol{X}), \boldsymbol{X})}{\partial \boldsymbol{F}} \tag{2.20}$$

Equation 2.20 followed by 2.17 is often used as a definition of a hyperelastic material [13]. When the material undergoes rigid body rotation Ψ must remain invariant, this implies that Ψ depends on $\boldsymbol{F}$ only via stretch component $\boldsymbol{U}$ and is independent of the rotation component $\boldsymbol{R}$. Therefore, Ψ is expressed as a function of $\boldsymbol{C} = \boldsymbol{U}^2 = \boldsymbol{F}^T\boldsymbol{F}$ as:

$$\Psi(\boldsymbol{F}(\boldsymbol{X}), \boldsymbol{X}) = \Psi(\boldsymbol{C}(\boldsymbol{X}), \boldsymbol{X}). \tag{2.21}$$

where $\boldsymbol{C}$ is right Couchy Green tensor.

The relation between the Green-Lagrange strain tensor($\boldsymbol{E}$) and the right Couchy Green tensor ($\boldsymbol{C}$) is written as $\boldsymbol{E} = \frac{1}{2}\boldsymbol{C} - I$. Therefore, the material derivative of this relation yields:

$$\dot{\boldsymbol{E}} = \frac{1}{2}\dot{\boldsymbol{C}} \tag{2.22}$$

Where $\dot{\boldsymbol{E}}$ is a work conjugate of second Piola-Kirchoff stress $\boldsymbol{S}$ enables a Lagrangian constitutive equation to be constructed as:

$$\dot{\Psi} = \frac{\partial \Psi}{\partial \boldsymbol{C}} : \dot{\boldsymbol{C}} = \frac{1}{2}\boldsymbol{S} : \dot{\boldsymbol{C}}; \qquad \boldsymbol{S}(\boldsymbol{C}(\boldsymbol{X}), \boldsymbol{X}) = 2\frac{\partial \Psi}{\partial \boldsymbol{C}} = \frac{\partial \Psi}{\partial \boldsymbol{E}} \tag{2.23}$$

This relation between the 2nd Piola-Kirchoff stress tensor and the right Cauchy-Green tensor $\boldsymbol{C}$ is non-linear.

The hyperelastic constitutive equations defined above are unrestricted in their application. To implement the case of isotropic material, it is important to ensure the constitutive behaviour is identical in any material direction. This means that the

relationship between Ψ and $\boldsymbol{C}$ must be independent of the material axes chosen, and therefore, Ψ must be a function of the invariants of $\boldsymbol{C}$ [13].

$$\Psi(\boldsymbol{C}(\boldsymbol{X}), \boldsymbol{X}) = \Psi(I_C, II_C, III_C, \boldsymbol{X}) \tag{2.24}$$

Where the invariants of $\boldsymbol{C}$ are defined as:
$I_C = tr\,\boldsymbol{C} = \boldsymbol{C} : \boldsymbol{I}$
$II_C = tr\,\boldsymbol{C}\boldsymbol{C} = \boldsymbol{C} : \boldsymbol{C}$;
$III_C = det\,\boldsymbol{C} = J^2$

Therefore, the second Piola-Kirchoff stress can be written as:

$$\boldsymbol{S} = 2\frac{\partial \Psi}{\partial \boldsymbol{C}} = 2\frac{\partial \Psi}{\partial I_C}\frac{\partial I_C}{\partial \boldsymbol{C}} + 2\frac{\partial \Psi}{\partial II_C}\frac{\partial II_C}{\partial \boldsymbol{C}} + 2\frac{\partial \Psi}{\partial III_C}\frac{\partial III_C}{\partial \boldsymbol{C}} \tag{2.25}$$

$$\boldsymbol{S} = 2\Psi_I \boldsymbol{I} + 4\Psi_{II}\boldsymbol{C} + 2J^2\Psi_{III}\boldsymbol{C}^{-1} \tag{2.26}$$

where Ψ_I=$\partial\Psi/\partial I_C$, Ψ_{II}=$\partial\Psi/\partial II_C$, and Ψ_{III}=$\partial\Psi/\partial III_C$.

Several particular forms of the strain energy potential are available, among them the relevant ones for this thesis are:

1. Neo Hookean form
2. Mooney-Rivlin form
3. Polynomial form

2.2.3.1 Compressible Neo-Hookean energy potential

The stored energy function of Neo-Hookean energy potential is defined as:

$$\Psi = \frac{\mu}{2}(I_C - 3) - \mu ln J + \frac{\lambda}{2}(ln J)^2 \tag{2.27}$$

where the constants λ and μ are material coefficients and $J^2 = III_C$. When there is no deformation, i.e., $\boldsymbol{C}$=$\boldsymbol{I}$, the stored energy function vanishes as expected.

The second Piola-Kirchoff stress can now be obtained from Equation 2.26 as:

$$\boldsymbol{S} = \mu(\boldsymbol{I} - \boldsymbol{C}^{-1}) + \lambda(ln J)\boldsymbol{C}^{-1}. \tag{2.28}$$

2.2.3.2 Mooney-Rivlin energy potential

The stored energy potential of Mooney-Rivlin material is defined as:

$$\Psi = \frac{\mu_1}{2}(I_C - 3) + \frac{\mu_2}{2}(II_C - 3) + \frac{\lambda}{2}(J - 1)^2 \tag{2.29}$$

where μ_1, μ_2, λ are material properties

2.2.3.3 Polynomial energy potential

The stored energy potential of polynomial form is defined as Equation 2.30 [14].

$$\Psi = \sum_{i+j=1}^{N} C_{ij}(I_C - 3)^i (II_C - 3)^j + \sum_{i=1}^{N} \frac{1}{D_i}(J-1)^{2i} \tag{2.30}$$

The parameter N can take values up to six; however, values of N greater than 2 are rarely used when both first and second invariants are considered. C_{ij} and D_i are material parameters.

2.2.4 Crushable foam response

Foams are structures which can absorb significant amounts of energy before failure, mostly impact energy. They are also used in cores of sandwich panels in lightweight structures. Foams can be seen in nature as well e.g., wood, which supports the tree or the cancellous bone which gives light and stiff frames to the animals [15]. The crushable foam material model is one of the important material models of this thesis. As discussed in the introduction chapter, the reduction in distance between the particles during compression and subsequent plastic deformation can be computationally modelled using the crushable foam material model [1].

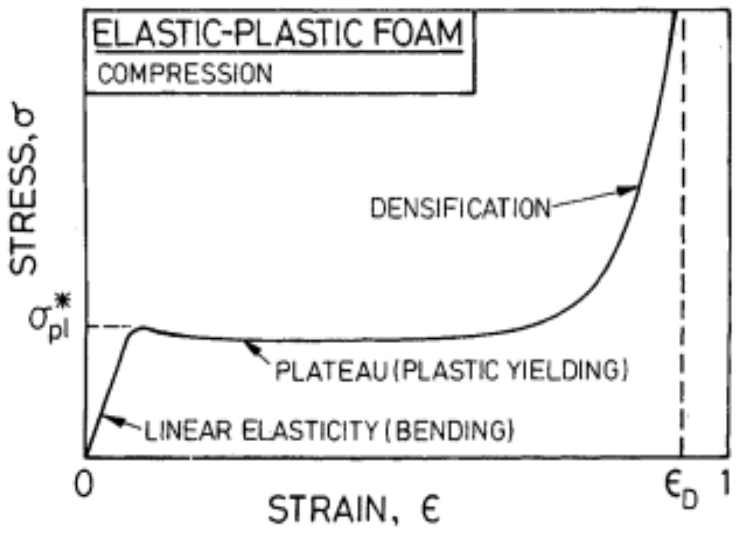

Figure 2.3: Crushable foam material response in the form of stress vs strain curve, adapted from [15].

The crushable material exhibits linear elasticity and a non-linear volumetric hardening plasticity illustrated in Figure 2.3.
The elastic part of the response is similar to the section 2.2.1. The stress-strain relationship can be expressed as

$$\boldsymbol{\sigma} = \mathbf{D}^{el} : \epsilon^{el} \tag{2.31}$$

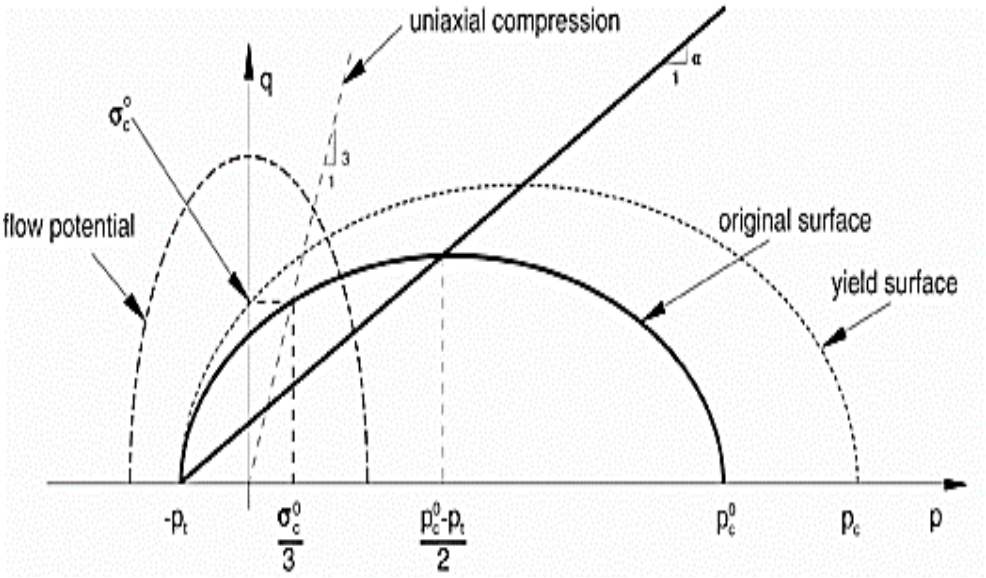

Figure 2.4: Crushable foam material model yield surface illustration, adapted from [14].

where $\boldsymbol{D}^{el}$ represents the fourth-order elasticity tensor and $\boldsymbol{\sigma}$ and ϵ^{el} are the second-order stress and elastic strain tensor, respectively.

For the plastic part of the behaviour, the yield surface is a Mises circle in the deviatoric stress plane and an ellipse in the meridional stress plane as seen in Figure 2.4. In the volumetric hardening model, the point on the yield ellipse which represents the hydrostatic tension (P_t) loading is fixed and the evolution of the yield surface is driven by the volumetric compacting plastic strains. The yield surface of the volumetric hardening model is defined as

$$F = \sqrt{q^2 + \alpha^2(p - p_o)^2} - B = 0 \tag{2.32}$$

$$p = -\frac{1}{3} trace(\boldsymbol{\sigma}) \tag{2.33}$$

$$q = \sqrt{\frac{3}{2}\boldsymbol{S} : \boldsymbol{S}} \tag{2.34}$$

$$\boldsymbol{S} = \boldsymbol{\sigma} + p\boldsymbol{I} \tag{2.35}$$

where, p is the pressure stress, q is the Mises stress, and $\boldsymbol{S}$ is the deviatoric stress. The shape factor α can be expressed as

$$\alpha = \frac{3k}{\sqrt{(3k_t + k)(3 - k)}} \tag{2.36}$$

where $k_t = \frac{P_t}{P_c^0}$ and $k = \frac{\sigma_c^0}{P_c^0}$. The yield surface intersects the p-axis at -P_t and P_c. It is assumed that P_t remains fixed throughout any plastic deformation process. The compressive strength, P_c, evolves as a result of compaction (increase in density) as shown in Figure 2.3 of the material. The evolution of the yield surface can be

expressed through the evolution of the yield surface size on the hydrostatic axis, P_t+P_c, as a function of the value of volumetric compacting plastic strain, -ϵ_{vol}^{pl} [14]. This relation can be written as

$$P_c(\epsilon_{vol}^{pl}) = \frac{\sigma_c(\epsilon_{axial}^{pl})[\sigma_c(\epsilon_{vol}^{pl})(\frac{1}{\alpha^2} + \frac{1}{9})] + \frac{P_t}{3}}{P_t + \frac{\sigma_c(\epsilon_{axial}^{pl})}{3}} \tag{2.37}$$

where ϵ_{axial}^{pl}=ϵ_{vol}^{pl} in uniaxial compression for the volumetric hardening model.

2.3 Homogenisation of the material properties

Homogenisation of the material properties is one of the most important aspects of this study. A homogenised material property is important when considering modelling a battery pack for a complete vehicle crash analysis, which is a real-life case. This study is limited to estimating the effective properties of a jellyroll. If all electrode layers and separators are modelled at the nanoscale even in the jellyroll model it requires a huge amount of computation time and therefore consumes more energy and becomes an expensive approach.

There are many different approaches to obtain homogenised properties of a material, the most relevant approaches are described in the following sections.

2.3.1 Finite element homogenisation using representative volume element

In this approach a representative unit is modelled, this unit should be such that it represents the periodicity of the material. An RVE is the smallest volume in the material which can be periodically translated into 3 dimensions and obtain the full scale material properties. The concept is similar to calculating the density of water from a small beaker instead of trying to calculate from a flowing river. In both cases, it will remain the same. Similarly, a material's response towards a certain mechanical load will remain the same irrespective of the size i.e., the elastic response of a material is based on the atomic interaction, in this case, for a constant volume fraction of the inclusions, it will remain the same at any scale. While considering an RVE it is also important to understand the concept of different boundary conditions and RVE size. While doing FE homogenisation it is important to observe the behaviour under different boundary conditions.

2.3.1.1 Dirichlet boundary conditions

This type of boundary condition, also known as homogeneous displacement boundary condition, implements uniform displacement over the external boundaries of the RVE in the absence of external body forces. This boundary condition will prescribe a prior value of displacement at the boundaries before the FEM simulation starts [16]. Figure 2.5(a) shows a virtual domain subjected to a uniform displacement in

the x direction, δ_x, on all right edge nodes while the opposite and the bottom edge are restricted in the x and y directions. Application of Dirichlet boundary conditions (DBCs) in the RVE for obtaining homogenised material properties requires slight modifications. To capture material response and extract the stiffness modulus in each direction, unit strain is applied as mentioned above in the form of displacement for each case. Equations 2.38-2.41 [12] show the DBCs for extracting stiffness response in all the directions mentioned.

$$\epsilon_1^0 = 1; \epsilon_2^0 = \epsilon_3^0 = \gamma_4^0 = \gamma_5^0 = \gamma_6^0 = 0 \tag{2.38}$$

$$\epsilon_2^0 = 1; \epsilon_1^0 = \epsilon_3^0 = \gamma_4^0 = \gamma_5^0 = \gamma_6^0 = 0 \tag{2.39}$$

$$\epsilon_3^0 = 1; \epsilon_1^0 = \epsilon_2^0 = \gamma_4^0 = \gamma_5^0 = \gamma_6^0 = 0 \tag{2.40}$$

$$\gamma_6^0 = \epsilon_{12}^0 + \epsilon_{21}^0 = 1; \epsilon_1^0 = \epsilon_2^0 = \epsilon_3^0 = \gamma_4^0 = \gamma_5^0 = 0 \tag{2.41}$$

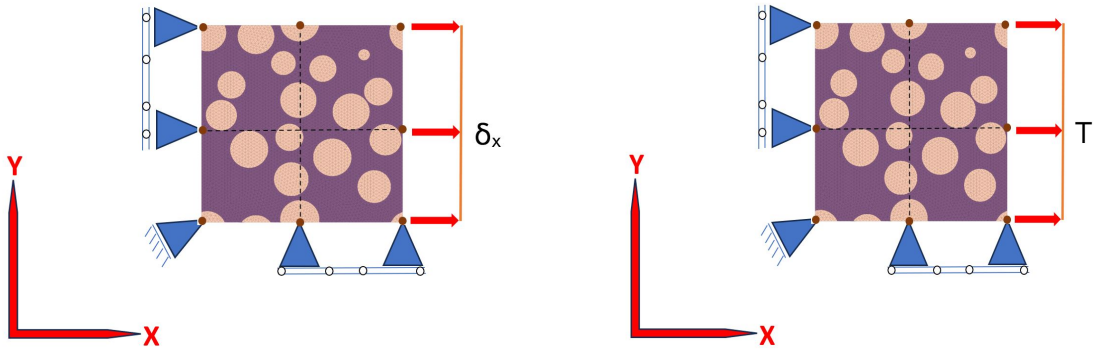

(a) **(b)**

Figure 2.5: **(a)** Figure showing the application of Dirichlet boundary condition also known as a displacement boundary condition, **(b)** Illustration of the Neumann boundary condition also known as a traction boundary condition.

2.3.1.2 Neumann boundary conditions

Neumann boundary conditions also known as static uniform boundary conditions implement uniform traction ($\mathbf{T}$) over the external boundaries of an RVE in the absence of an external displacement vector. Neumann BC can be defined over a domain, $\partial\Omega$, which has an outward normal vector, $\mathbf{n}$, for a domain variable, ζ, thus: $\frac{\partial\zeta}{\partial\mathbf{n}} \equiv \alpha$, where α = constant [16]. Figure 2.5(b) illustrates this type of boundary condition where $\mathbf{T}$ represents traction which is the normal derivative of force, i.e., $\mathbf{T} = \frac{\partial\mathbf{F}}{\partial\mathbf{n}}$

2.3.1.3 Periodic boundary conditions

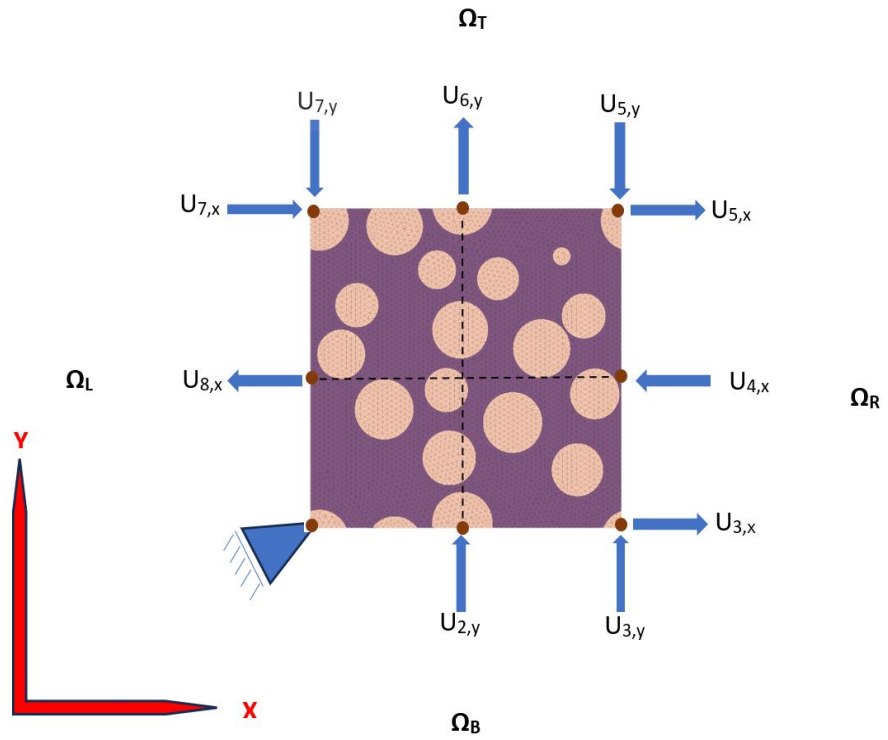

Figure 2.6: PBC demonstration on four different edges of a 2D square which are kinematically tied to follow each other.

The periodic boundary condition (PBC) constraints the opposite pair of edges or surfaces on the boundary of an RVE to deform identically under a given loading condition. Figure 2.6 shows a 2D RVE of a heterogeneous material subjected to uniaxial tensile deformation and imposed with PBCs. The figure shows that the material has nodes $N1$ to $N8$ and the 2D RVE virtual domain is bounded by the boundary $\Omega \subset \Re^n$. The definition of Ω is illustrated in Equation 2.42 [16].

$$\Omega = \Omega_L \cup \Omega_R \cup \Omega_T \cup \Omega_B \tag{2.42}$$

The subscript L, R, T, B corresponds to left, right, top and bottom. Hence, the PBCs make sure that the deformation profile of the left boundary Ω_L must deform equivalent to the right boundary, Ω_R. Similarly, the deformation profile should match in shape and value for the top Ω_T and the bottom Ω_B boundary [16]. Mathematically, the PBC of a model variable, ζ on boundary Ω_k can be defined as:

$$\zeta^{N_a}_{(x,y)} = \zeta^{N_b}_{(x,y)} \tag{2.43}$$

where N_a and N_b are kinematically linked on the opposite edges and k=L, R, T, B.

Mathematical Formulation for PBCs:

Figure 2.7 below shows a 2D RVE of the micro-structure of a particulate composite represented by domain $\Omega \subset \Re^n$. The domain is divided into sub-domains which

correspond to left, right, top and bottom edges of the RVE, respectively. The domain also has four corner nodes, N_1, N_2, N_3, and N_4 and four internal /reference nodes N_A, N_B, N_C, and N_D. It is rigidly fixed at the node N_1 to prevent rigid body motion.

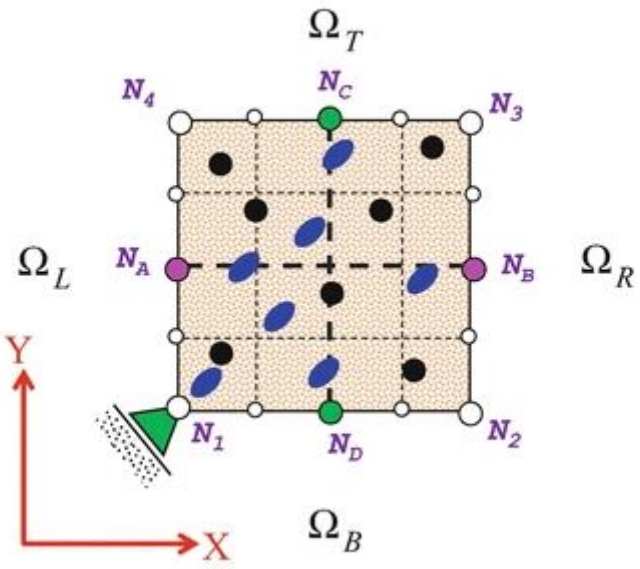

Figure 2.7: Figure to illustrate the different nodes on different edges of a 2D square to demonstrate the constraints of PBCs [16]

The PBC ties the reference nodes kinematically to the homogeneous deformation of the corner nodes. The PBC implementation for the displacement of the reference nodes can be written as:

$$\mathbf{U}_{(x,y)}^{N_B} = \mathbf{U}_{(x,y)}^{N_A} \Rightarrow \mathbf{U}_{(x,y)}^{N_B} - \mathbf{U}_{(x,y)}^{N_A} = 0 \tag{2.44}$$

$$\mathbf{U}_{(x,y)}^{N_C} = \mathbf{U}_{(x,y)}^{N_D} \Rightarrow \mathbf{U}_{(x,y)}^{N_C} - \mathbf{U}_{(x,y)}^{N_D} = 0 \tag{2.45}$$

Similarly, the displacement of the corner nodes can be written as:

$$\mathbf{U}_{(x,y)}^{N_2} = \mathbf{U}_{(x,y)}^{N_1} \Rightarrow \mathbf{U}_{(x,y)}^{N_2} - \mathbf{U}_{(x,y)}^{N_1} = 0 \tag{2.46}$$

$$\mathbf{U}_{(x,y)}^{N_4} = \mathbf{U}_{(x,y)}^{N_1} \Rightarrow \mathbf{U}_{(x,y)}^{N_4} - \mathbf{U}_{(x,y)}^{N_1} = 0 \tag{2.47}$$

where $U_{(x,y)}^{N_A}$ and $U_{(x,y)}^{N_1}$ are the nodal displacement vector of node N_A and N_1, respectively in x and y direction. Node N_3 is excluded from the list of retained nodes as its deformation is influenced by the deformation of nodes N_2 and N_4. Node N_3 is commonly regarded as a slave/dummy node [16].

In the case of this thesis, the study is done to extract the stiffness response of the material and therefore it is important to apply strain in the corner/retained nodes

to stress the material and therefore obtain the elastic response. This can be done by introducing known DBCs, say δ_x on any of the retained nodes. As a result, the deformation of any retained nodes will follow the mathematical formulation of Equations 2.44, 2.45, and 2.46. Therefore, by equating Equation 2.44 to 2.46 and Equation 2.45 to 2.47 following equations are obtained based on which PBC is imposed:

$$\mathbf{U}^{N_B}_{(x,y)} - \mathbf{U}^{N_A}_{(x,y)} - \mathbf{U}^{N_2}_{(x,y)} + \mathbf{U}^{N_1}_{(x,y)} = 0 \tag{2.48}$$

$$\mathbf{U}^{N_C}_{(x,y)} - \mathbf{U}^{N_D}_{(x,y)} - \mathbf{U}^{N_4}_{(x,y)} + \mathbf{U}^{N_1}_{(x,y)} = 0 \tag{2.49}$$

2.3.2 Analytical Homogenisation

Analytical homogenisation is another relevant homogenisation approach in the scope of this thesis. Unlike homogenisation using the RVE, analytical homogenisation is independent of the size/volume of the material. It takes into consideration the material properties of the individual constituents and their volume fractions, respectively. Based on assumptions of stress and strain, Voigt and Reuss upper and lower bound values of the elastic stiffness can be obtained. The analytical models yield formulas for the stiffness $\mathbf{C}$ and compliance $\mathbf{S}$ tensor of the composite such as :

$$\mathbf{C} = \sum V_i \mathbf{C}^i \mathbf{A}^i; \quad \sum V_i \mathbf{A}^i = \mathbf{I} \tag{2.50}$$

$$\mathbf{S} = \sum V_i \mathbf{S}^i \mathbf{B}^i; \quad \sum V_i \mathbf{B}^i = \mathbf{I} \tag{2.51}$$

where:

- V_i represents the volume fraction of the i-th phase in the composite.
- $\mathbf{C}^i$ represents the stiffness tensor of the i-th phase.
- $\mathbf{S}^i$ represents the compliance tensor of the i-th phase.
- $\mathbf{A}^i$ and $\mathbf{B}^i$ are the stress and strain concentration tensors of the i-th phase, respectively.
- $\mathbf{I}$ is the 6×6 identity matrix.

Furthermore, for particle-reinforced polymer composites, $i = p, m$ represents the particle and the matrix phases, respectively [12].

2.3.2.1 Reuss Lower Bound

The Reuss model assumes that the stress tensors in the constituents, and composite are the same $\boldsymbol{\sigma} = \boldsymbol{\sigma}^p = \boldsymbol{\sigma}^m$; so, the stress concentration tensors are all equal to the 6×6 identity matrix $\mathbf{A}^i = \mathbf{I}$. This yields the lower limit of the elastic stiffness of the system [12].

2.3.2.2 Voigt Upper Bound

The Voigt model assumes that the strain tensors in the constituents and composite are the same $\boldsymbol{\epsilon} = \boldsymbol{\epsilon}^p = \boldsymbol{\epsilon}^m$; so the strain concentration tensors are equal to the 6×6 identity matrix $\mathbf{B}^i = \mathbf{I}$. This yields the upper limit of the elastic stiffness of the system [12].

3
Methods

3.1 Numerical homogenisation of the material properties at nanoscale

The numerical homogenisation method involves analysing an RVE under specific boundary conditions to extract the stiffness response of the material. To begin with, the homogenisation of the material properties of all the constituents; electrodes, separator, and current collectors, are assumed to be linear elastic. This approach is done to first develop the modelling strategy and allow more complex material models to be implemented when needed.

The linear elastic homogenisation approach involves running an FE simulation of the RVE to extract the individual columns of the 6X6 stiffness matrix as seen in equations 2.3 and 2.4.

3.1.1 Linear elastic RVE modelling of the electrodes and separator

This study extensively relies on RVE modelling and its analysis for FE homogenisation. The RVE analysis is first done on the nanoscale as shown in Figure 1.4, where the individual layers of the battery cell, e.g., electrodes, and separators are modelled and their homogenised properties are extracted. This process gives robustness to the modelling strategy since the model is built on the properties of individual constituents within the layers.

An RVE is the smallest representative volume which can demonstrate the properties of the entire material. Therefore, an RVE of the smallest size saves a lot of computation time. In the linear elastic RVE modelling for the electrodes and the separator, the properties are taken from Table 3.1.

To create the RVEs, the commercial software ANSA Version 24.1.0 has been used. This software has a built-in tool named "RVE Generator", which takes input in the form of e.g., material properties of the matrix and particles, volume fractions and RVE dimensions. The RVE of the electrodes and the separator is based on the volume fraction and size of the electrodes and separator inside the battery cell. By selecting the short fibre distribution and putting the values of the radius and the length of the fibres as the radius of the particles/pores mentioned in Table 3.2, it

Table 3.1: Mechanical properties of the constituent materials of the battery (electrodes and separator).

Material	Elastic Modulus (GPa)	Poisson's Ratio μ (-)	Shear Modulus (GPa)	Reference
LFP	124	0.28	48.4	[17]
Graphite	32	0.32	12	[17]
PVDF-CB-Electrolyte system	9.5	0.3	3.65	[18]
Separator (PE)	0.7	0.35	0.26	[19]

creates an RVE with volume fraction feasible for the given case as seen in Figure 3.1(a). However, to obtain the desired volume fraction it is important to have a varied size of the particles, which is the case in reality. To do that, there is the possibility to create different inclusions inside the ANSA RVE tool.

Table 3.2: Description of the input parameters used to build the RVE of the particles reinforced polymer matrix system of electrodes and the porous separator.

Electrodes/ separator	RVE size (μm)	Volume fraction of the particles (%)	particle/pore radius (μm)
Cathode	40	30	2.5
Anode	40	30	2.5
Separator	40	30	2.5

In the case of the RVE model of the separator, a random distribution of the inclusions with negligible stiffness is used. This helps to mimic the porous nature of the separator, illustrated in Figure 3.1(b). Since the stiffness of the inclusion is almost equal to zero numerically, it has negligible influence on the load-bearing capability of the RVE. It is noted that only quasi-static loading conditions are explored at this point.

The meshing for this case is done using the same tool "RVE Generator". Since it is a simple RVE problem with linear elastic material properties, a C3D4 element is selected, which is a 4-node linear tetrahedron element.

3.1.1.1 RVE convergence study for the linear elastic response

Representative volume elements modelling is one of the important aspects of material characterisation in this thesis. Therefore, an iterative study has been carried out to validate the existing numerical results. In the 2nd iteration of the numerical RVE modelling, the same tool as in the first iteration is used, i.e., ANSA RVE Generator,

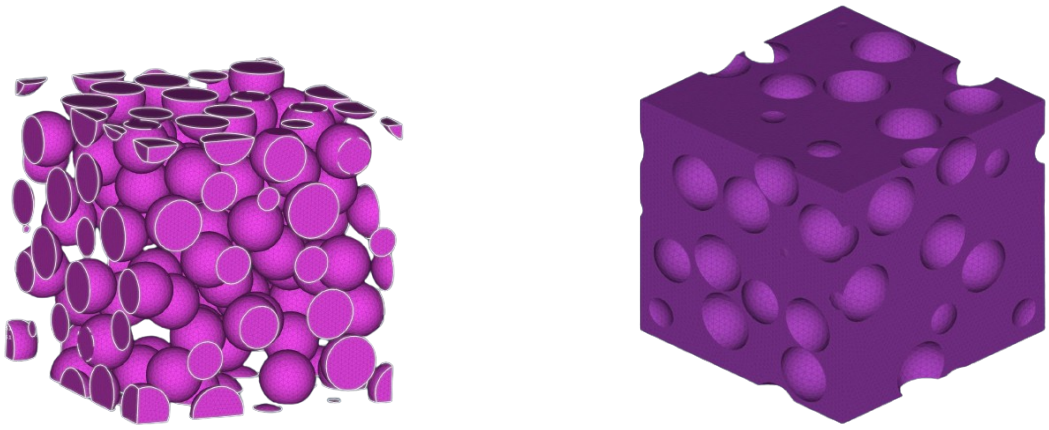

(a) **(b)**

Figure 3.1: **(a)** Particle distribution using ANSA inbuilt tool RVE Generator, these particles are solid meshed inside the tool itself, **(b)** RVE of the separator using ANSA inbuilt tool RVE Generator

but this time version 24.0.1 is used instead of 24.1.0.

In this model, different boundary conditions as mentioned in subsection 2.3.1.1 and 2.3.1.3, are implemented. The results from their analysis are compared to understand the significance of different boundary conditions as well as the behaviour of the RVE. Apart from the solver Abaqus, one more solver is used, called MSC Nastran. To check the size dependency of the RVE various sizes of the RVE are modelled. This analysis helps in identifying the smallest RVE size which can be further used in this study. A description of the changes made in the RVE models is listed in Table 3.3. It is worth noting that throughout the changes made in the models, mesh size and element type are kept constant. This is done to eliminate the mesh dependency of the results.

Table 3.3: Description of the changes done to perform RVE convergence study

Battery parts	**RVE size in model 1(μm)**	**RVE size in model 2(μm)**	**RVE size in model 3(μm)**	**RVE size in model 4(μm)**	**RVE size in model 5(μm)**	**Mesh size (μm)**
Cathode	40	22	10	7	5.3	0.5
Anode	40	22	10	7	5.3	0.5
Separator	40	22	10	7	5.3	0.5

3.1.2 Analysis of the linear elastic RVE model at nanoscale

The RVE models created using the pre-processing software ANSA, are written as an input file for solver available in the commercial software; Abaqus and MSC Nastran.

These files can be directly imported into the simulation software for analysis. The changes in the model can be seen in Table 3.3.

3.1.2.1 Simulation of the RVE using DBCs

The RVE model is simulated under 4 different boundary conditions to extract the material response of the particle-reinforced polymer matrix system. Equations 2.38-2.40 are implemented in Abaqus CAE using the symmetric boundary conditions on each face. To obtain the unit strain in 1, 2, or 3 directions, a displacement load is applied accordingly in X, Y and Z directions. The corresponding Abaqus input file command for one of the cases of simulation (to extract the 2^{nd} column of the stiffness matrix) can be seen in the Listing 3.1. Subsequently Equations 2.5-2.10 were used to extract the Young's modulus and shear modulus respectively.

Listing 3.1: Boundary condition definition implementing Equation 2.39 for linear elastic RVE modelling of the electrodes and separator

```
** BOUNDARY CONDITIONS
** Name: Disp-BC-1 Type: Displacement/Rotation
*Boundary
SET-46, 2, 2, 40.
** Name: Disp-BC-2 Type: Symmetry/Antisymmetry/Encastre
*Boundary
SET-42, XSYMM
** Name: Disp-BC-4 Type: Symmetry/Antisymmetry/Encastre
*Boundary
SET-44, YSYMM
** Name: Disp-BC-6 Type: Symmetry/Antisymmetry/Encastre
*Boundary
SET-41, ZSYMM
```

Implementing Equation 2.41 is a bit more complicated. To achieve only distortion strain it is important to lock both the faces of the Z direction. This is done by defining tie constraints on Z faces, and symmetric boundary conditions in the X direction. One of the faces of the Y direction is given a displacement vector in the Z direction while keeping the other face restricted to move in the X direction. This complete system of boundary conditions creates an environment to execute Equation 2.41 and obtain the shear response of the material in the YZ direction.

3.1.2.2 Simulation of the RVE using PBCs

To implement PBCs for the linear elastic RVE model, ANSA"RVE Generator" is used. This tool also allows solving the RVE problem inside the software itself with the built-in plug-in of Epylisis, a MSC Nastran-based solver. The system creates 6 sub-cases which deal with obtaining the 6 columns of the stiffness matrix. Each sub-case creates displacement in certain nodes in X, Y, Z, XY, YZ, and XZ directions to solve for 3 mutually perpendicular directions and 3 shear deformation cases. The solver also performs homogenisation based on the user input of isotropic, orthotropic, and transversely isotropic material characteristics. In this study, isotropic homogenisation of the electrodes and separator RVE is done.

3.1.3 Hyperelastic RVE modelling of the electrodes

The previous steps were performed to establish the material modelling strategy of the RVE of various sizes and a very simple linear elastic material model was implemented. However, it is worth noting that the combined response of the PVDF binder with carbon black and the liquid electrolyte in the nanopores of the PVDF is expected to be highly non-linear and the modelling of this multi-phase system is complex. Therefore, the matrix is considered as a combined system in this study. In the first iteration, this matrix system is considered as Neo-Hookean material and the particles are still considered linear elastic. Hence, slightly softer material properties are implemented for this combined system, which are Listed in Table 3.4.

Table 3.4: Description of the input parameters used to build the hyperelastic RVE of the particles reinforced polymer matrix system of electrodes and the porous separator.

Material	**Young's modulus, E (GPa)**	**Poisson's ratio, ν (-)**	**Shear modulus, G (GPa)**	**Bulk modulus, K (GPa)**	C_{10} **(GPa)**	D_1 **(GPa^{-1})**
Matrix system	1	0.4	0.36	1.67	1.78e-5	1.19e3

In this case, to address the realistic particle distribution, the volume fraction is increased both in the case of the LFP-matrix system and the graphite-matrix system. The complete changes in the models are listed in Table 3.5 and the new RVEs are shown in Figure 3.2. As seen in Figure 2.1, LFP and graphite particle sizes are not the same throughout the volume. Therefore, two different sizes of both LFP and graphite particles are created to achieve the desired volume fraction. In addition to that, it is also difficult to mesh the RVE with a higher volume fraction just by implementing a single-size particle distribution.

The meshing of the hyperelastic material model is an important aspect. It is important to consider hybrid elements, therefore C3D4H elements are selected. C3D4H is a 4-node linear tetrahedron, hybrid, linear pressure element. To make sure the solver respond to the hyperelastic material it is important to turn on the geometric non-linearity feature (Nlgeom) while creating a displacement-driven load case step. To understand the complete hyperelastic behaviour of the matrix system the RVE is simulated for both tension and compression.

3.1.4 Analysis of the hyperelastic RVE model of the electrodes

The analysis of the hyperelastic model is done using Abaqus. The matrix system is considered to follow Neo-Hookean strain energy potential, which is a reduced polynomial strain energy function of order 1. Abaqus takes input in the form of Equation 3.1 [14] to solve this particular problem.

$$U = C_{10}(\bar{I}_1 - 3) + \frac{1}{D_1}(J_{el} - 1)^2 \tag{3.1}$$

Equation 3.1 is a modified version of equation 2.27 which Abaqus implements in its solver. The parameters C_{ij} and D_i are material parameters and in the case of a Neo-Hookean material, $C_{10}=\frac{\mu}{2}$ and $D_1=\frac{2}{k_0}$. In this model, μ and k_0 are the shear modulus (G) and bulk modulus (K) of the material, respectively. Further, $\bar{I}_1$ is first strain invariant and J_{el} is elastic volume strain.

Table 3.5: Description of the input parameters used to build the hyperelastic RVE of the particles reinforced polymer matrix system of electrodes.

Electrodes constituents	**RVE size (μm)**	**Volume fraction of the particles, v_1 and v_2 (%)**	**Particle radius, r_1 and r_2 (μm)**
Cathode	6	v_1=30; v_2=18	r_1=2.5; r_2=1
Anode	6	v_1=27; v_2=14.8	r_1=3; r_2=2.5

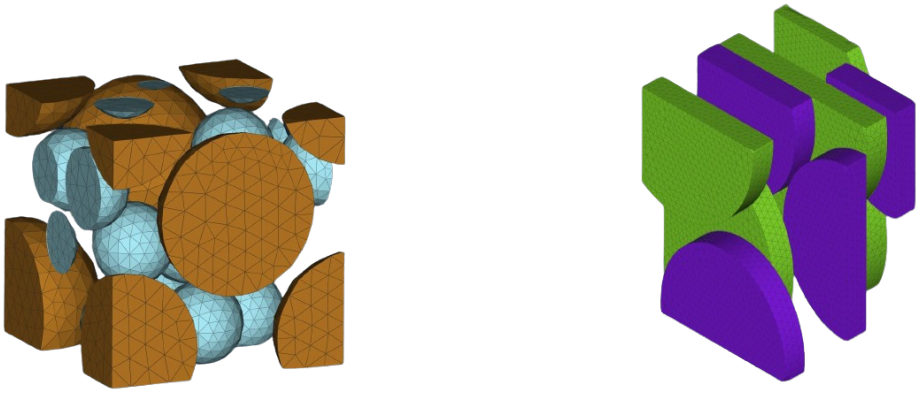

(a) **(b)**

Figure 3.2: **(a)** LFP Particle distribution with total volume fraction of 48%. **(b)** Graphite particle distribution with total volume fraction of 42%.

3.1.5 Modelling and simulation of the 2nd separator model

The separator in reality typically has a porosity of volume fraction of 40% [19]. Therefore, to address this, more realistic modelling of the separator is done. The implemented changes in the separator are listed in Table 3.6. As mentioned earlier, achieving a higher volume fraction of inclusions/pores just by using single-size

pores is difficult. Therefore, two different pore sizes are implemented in the model. For simplicity, the material response of the separator is set as linear elastic. The homogenisation is done using Epylisis inside ANSA.

Table 3.6: Description of the input parameters used to build the linear elastic RVE of the porous separator

Battery constituent	**RVE size (μm)**	**Volume fraction of the pores, v_1 and v_2 (%)**	**Pore radius, r_1 and r_2 (μm)**
Separator	5.2	v_1=30; v_2=13.4	r_1=0.9; r_2=0.5

3.2 Analytical homogenisation of the material properties at nanoscale

The analytical homogenisation is done for the linear elastic RVE model only. Similar to RVE generation, the RVE tool in ANSA is used for analysis. For this particular case, a tool named, "Meanfield Homogenisation" is used. This tool has the feature to directly import the RVE properties generated using the tool "RVE Generator". The tool takes user input regarding the homogenisation scheme solving the problem. It is possible to solve a wide range of analyses, however linear elasticity is used for the current study. For all the cases of the RVE convergence study, both Voigt upper bound and Reuss lower bound values are also obtained using this software.

3.3 Numerical homogenisation of material properties at microscale

The numerical homogenisation at the microscale corresponds to the RVE analysis of the stack (layers of electrodes, separator and current collectors). This is a very important stage before proceeding to the full-scale modelling of the jellyroll. This stage is the intermediate stage in this study. Since the repeated unit of the jellyroll is a stack, in other words, a stack is considered representative of the jellyroll. Therefore, it is important to understand the homogenised response of the stack.

3.3.1 Linear elastic RVE modelling of the stack

The linear elastic RVE modelling of the stack is done using the pre-processing software ANSA. In this case, a simple test model is created, where only one cathode, one anode and one separator are used as seen in Figure 3.3. Hexa elements of size 5 μm are used in the model. It is created in the software and imported to the "RVE Generator" tool, where it is possible to apply PBCs to the model.

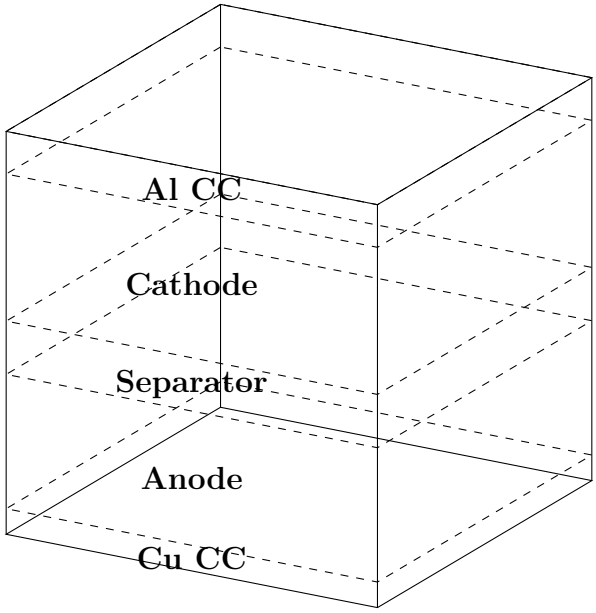

Figure 3.3: RVE of the stack with single side electrode coating, with an overall size of 189 μm, where the copper current collector (Cu CC) is 12 μm, aluminium current collector (Al CC) is 20 μm, cathode is 69 μm, anode is 63 μm and the separator is 25 μm [1].

3.3.2 Analysis of the linear elastic RVE model of the stack

The analysis of the linear elastic RVE model of the stack is done similarly to the linear elastic analysis of the electrodes. The analysis is done using both DBCs and PBCs. To perform homogenisation using DBCs, similar boundary conditions as mentioned in the section 3.1.2.1 are applied in Abaqus CAE. The solved files are imported into the RVE tool of ANSA and case by case 6 columns of the orthotropic stiffness matrix are obtained.

Similar approaches as section 3.1.2.2 are obtained when implementing PBCs for the stack. However, in addition to MSC Nastran, Abaqus is also used to solve the linear elastic problem using PBCs. The PBC is applied using the RVE tool in ANSA for both Abaqus and MSC Nastran. The corresponding command for the Abaqus input file for PBCs can be seen in the Listing 3.2. A total of 38643 equations linked to the number of degrees of freedom in the model are solved to execute the PBC in Abaqus. To homogenise the material response, again the model is imported into the ANSA RVE tool and case by case 6 columns of the orthotropic stiffness matrix are extracted.

Listing 3.2: Input file command for implementing PBC in the stack

```
1 *Equation
2 3
3 EqnSet-1, 3, 1.
4 EqnSet-2, 3, -1.
5 EqnSet-3, 3, -1.
```

3.3.3 Hyperelastic RVE modelling of the stack

The hyperelastic modelling of the stack is done based on the homogenised hyperelastic response at the nanoscale. As mentioned earlier, the matrix system is considered as Neo-Hookean material and the reinforced particles are considered as linear elastic material. Therefore, their combined response towards compression and tension is an important factor in determining the material model to be used in the stack. The combined stress and strain data for compression and tension are used to find the best energy potential form from the hyperelastic material model. A total of 3 different energy potentials were checked to fit the test curve, namely; Neo-Hookean energy potential, Mooney Rivlin energy potential and 2^{nd} order polynomial energy potential. The calibration is done using the built-in material calibration tool of Abaqus CAE. The calibration tool gives output in the form of C_{ij} and D_i. These material parameters are the input of the selected energy potential and are case-based and calibrated to fit the input test curve. This process is done for both anode and cathode and the results are used to model the respective anode and cathode coating in the stack RVE. The metallic current collectors and the separator are treated as linear elastic at this stage for simplicity.

In the case of the hyperelastic material model of the stack, more realistic modelling is done as illustrated in Figure 3.4. There are two electrode coatings on the current collector. The model's dimensions are also changed compared to the linear elastic model. The complete model is prepared in the commercial software ANSA. However, the "RVE Generator" tool is not implemented in this model. During the study, it was observed that the tool does not support hyperelastic modelling of the RVE, nor does it support hyperelastic homogenisation of the model.

The meshing is done using C3D8H, which is a hybrid, linear pressure 8-node hexa element.

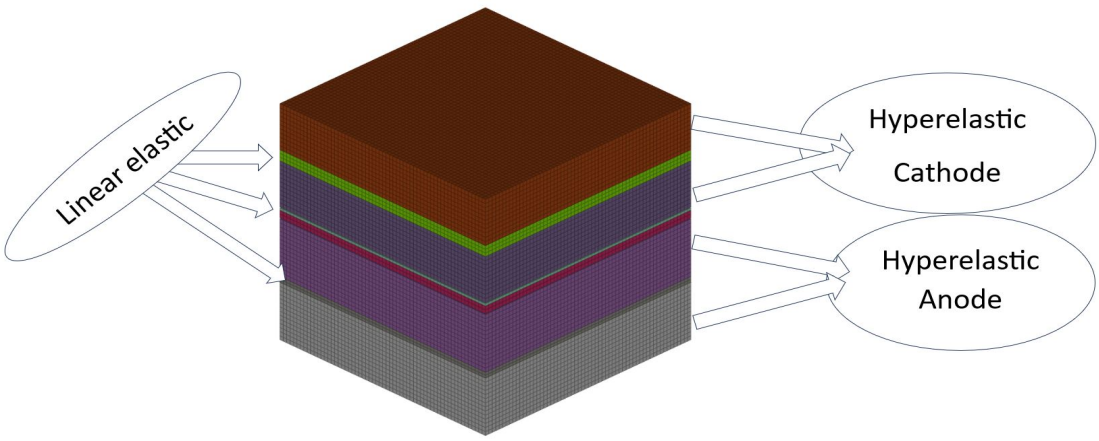

Figure 3.4: Modified stack RVE illustrating different material models being used, which are a hyperelastic model for the cathode and anode and a linear elastic model for the metallic current collectors and the separator.

3.3.4 Analysis of the hyperelastic RVE model of the stack

The simulation of the modified RVE of the stack is done in Abaqus using modified DBCs. It is important to understand the fact that during the compression of hyperelastic material for large deformation, it is likely that the convergence will be achieved without allowing the material to expand in either of the two directions. Therefore, out of the total of 6 faces, two in each X, Y and Z direction, only one of the faces of X, Y and Z are fixed with symmetric boundary conditions. However, one of the Z faces is given a displacement vector to achieve out-of-plane compression. This complete system of boundary conditions allows the simulation to achieve convergence for complex models as shown in Figure 3.4.

The homogenisation is done using Abaqus CAE, where stress and logarithmic strains are calculated at each integration point throughout the volume of the RVE. Abaqus stores the stress and strain values at all the integration points and calculates the average. This process plots the overall homogenised response of the RVE as an integrated compound material. The results are then exported to Excel using the built-in Excel plug-in available in Abaqus CAE.

3.3.5 Crushable foam modelling and analysis of the stack RVE

The crushable foam modelling of the stack is very similar to the modelling done for the hyperelastic stack. The difference lies in the element formulation and the material card. Unlike in the hyperelastic model, in the crushable foam model C3D8R element is chosen, it is an 8-node linear brick, reduced integration with the hourglass control element. This element formulation is chosen based on the literature research [1].

The material properties of this model are very important and play a vital role. It is very important to understand the solving process of Abaqus for the crushable foam material model. It takes input in the form of Young's modulus, Poisson's ratio, compression yield stress ratio and hydrostatic yield stress ratio. The latter two are explained as k and k_t in the section 2.2.4. Abaqus also requests to choose either foam hardening or the rate-dependent hardening mechanism. Since the rate-dependent study is not the scope of this thesis, foam hardening is chosen. The difference between these two mechanisms lies in the fact that in foam hardening, the user defines the behaviour of the material in the plastic zone by giving input in the form of plastic stress and corresponding plastic strain values. However, in the case of the rate-dependent hardening, the user selects a hardening law which then calculates the values of the plastic stress and strain for the given case. The detailed description of the material properties is illustrated in Table 3.7 and Figure 3.5. The homogenisation is done similarly to the hyperelastic material model.

The crushable foam material model used in this thesis is isotropic. The are possibilities to do an anisotropic crushable foam material model, however, the goal of this

thesis is to develop the methodology for the virtual testing of the batteries. In addition to that the corresponding validation stage includes a comparison of the force vs displacement values of the simulation and the test data. The test data values are in a uniaxial global coordinate system.

Table 3.7: Description of crushable foam material properties for the modelling of the stack RVE [1].

Electrode	**Young's modulus (GPa)**	**Poisson's ratio, ν (-)**	$\boldsymbol{k}$	$\boldsymbol{k}_t$
Cathode	1.6	0.01	1	600
Anode	0.5	0.01	1	400

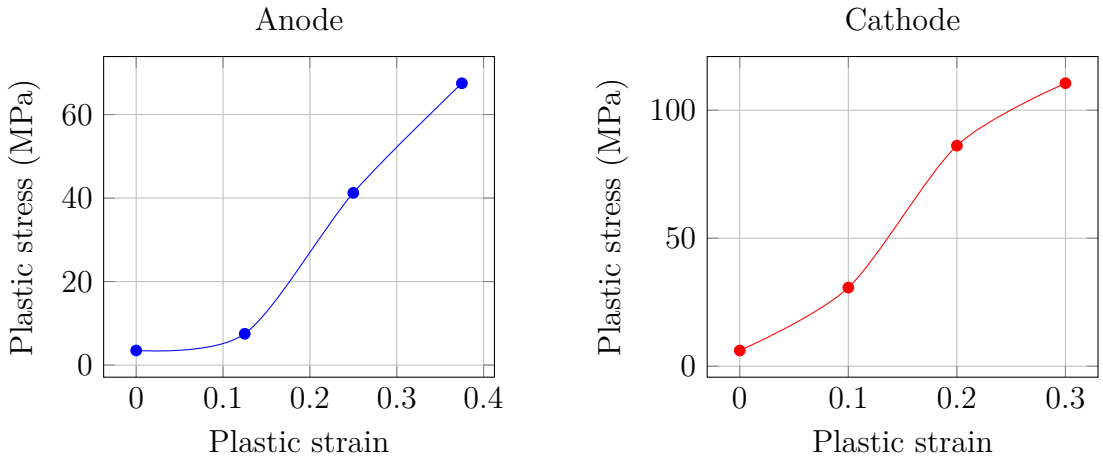

Figure 3.5: Plastic stress and strain data for anode (left) and cathode (right) which is an input to the volumetric foam hardening mechanism in Abaqus, adapted from [1].

3.4 Analytical homogenisation of the material properties at microscale

Analytical homogenisation of the material properties at the microscale is also done using the same tool "Meanfield Homogenisation" tool in commercial software ANSA. This process is quite similar to analytical homogenisation at the nanoscale. However, the RVE is built externally and imported to the homogenisation tool in this case. Like the microscale, both Voigt and Reuss's upper and lower bound of Young's modulus are checked.

3.5 Modelling and analysis of the metallic current collectors

The modelling of the metallic current collector is case-based. The element formulation changes based on the material model of the electrodes. If the hyperelastic material model is used for the electrodes, the element formulation for the metallic current collectors is C3D8H, which is a hybrid hexa element with 8 nodes. Similarly, if a crushable foam material model is used for the electrodes, the metallic current collector's element formulation is C3D8R, which is an 8-node reduced integration element. The current collectors are assigned isotropic hardening, the detailed description of the input parameters are illustrated in Table 3.8.

Table 3.8: Description of current collector material properties for the modelling of the stack RVE [20].

Current collector	**Young's modulus (GPa)**	**Poisson's ratio, ν (-)**	**Hardening**	**Yield stress (MPa)**
Copper	110	0.3	Isotropic	33
Aluminium	68	0.36	Isotropic	276

3.6 Material Modelling of the jellyroll using hyperelastic and crushable foam material model

The model of the jellyroll seen in Figure 3.6 is done in ANSA. It is modelled exclusively to run in LS-Dyna explicit solver. A material card is created separately which is called while running the simulation. MAT_077h, a hyperelastic material card and MAT_63, a crushable foam material card are used.

MAT_077h takes input in the form of order of the polynomial energy potential, and the LCID1 which is load curve ID1, by setting SGL (Specimen Gauge Length), SW (Specimen width), ST (Specimen Thickness) as unity, LCID1 takes input in the form of engineering stress and engineering strain.

MAT_63 takes input in the form of LCID which is a compressive plastic stress vs plastic strain curve, starting with compressive yield strength and corresponding plastic strain as zero.

The model has velocity-driven boundary conditions such that the rigid semi-spherical indenter moves 1 mm/ms. A detailed explanation of the complete modelling is illustrated in the thesis work of A. Purantagi, "Prediction of short-circuit of Li-ion battery cells during mechanical abuse".

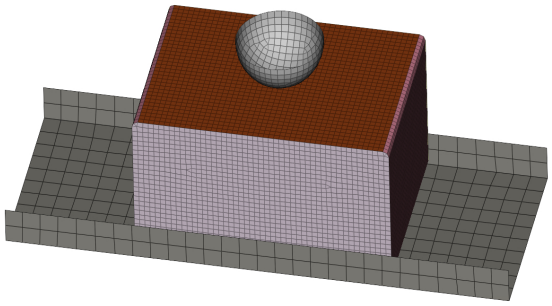

Figure 3.6: Jellyroll model with cell case used for validation step of the material models.

4

Results and discussion

This chapter focuses on the results obtained in this thesis. The homogenised response of RVE models at the nanoscale and microscale under different loading conditions and modelling strategies are presented. The resulting response is then utilised in model calibration to be used in the microscale modelling of the stack RVE. Concurrently the results of the homogenised response of the stack are shown. Finally, the full-scale jellyroll model results are explained.

4.1 Linear elastic numerical homogenisation of the material properties at the nanoscale

The linear elastic numerical homogenisation produces the stiffness matrix and accordingly, Young's modulus and Poisson's ratio of the material are extracted.

4.1.1 Homogenised response of the cathode using DBCs

Figure 4.1 shows the induced stress in 23 and 22 direction, simulated to obtain the homogenised response of the cathode. Figure 4.2 shows the individual response of the matrix and the LFP particles together with the homogenised response of the system.

The homogenisation of the simulated model yields similar C_{11}, C_{22} and C_{33} values, which correspond to E_1, E_2 and E_3 as seen in Equation 4.1. Since these results correspond to isotropic material only, one shear load case is simulated to extract the shear modulus G_{23} of the material. The linear elastic material properties of the cathode are summarised in Table 4.1. The Young's modulus of the system is quite low compared to the Young's modulus of the LFP particles (see Table 3.1). This suggests that the mechanical response of this system of composite material is matrix-dominated, which is typically the case when particles are embedded in the polymer matrix.

$$C_{ij} = \begin{bmatrix} 23.35 & 8.58 & 8.63 & 0 & 0 & 0 \\ 8.58 & 23.36 & 8.65 & 0 & 0 & 0 \\ 8.63 & 8.65 & 23.26 & 0 & 0 & 0 \\ 0 & 0 & 0 & 7.46 & 0 & 0 \\ 0 & 0 & 0 & 0 & 7.46 & 0 \\ 0 & 0 & 0 & 0 & 0 & 7.46 \end{bmatrix} (GPa) \tag{4.1}$$

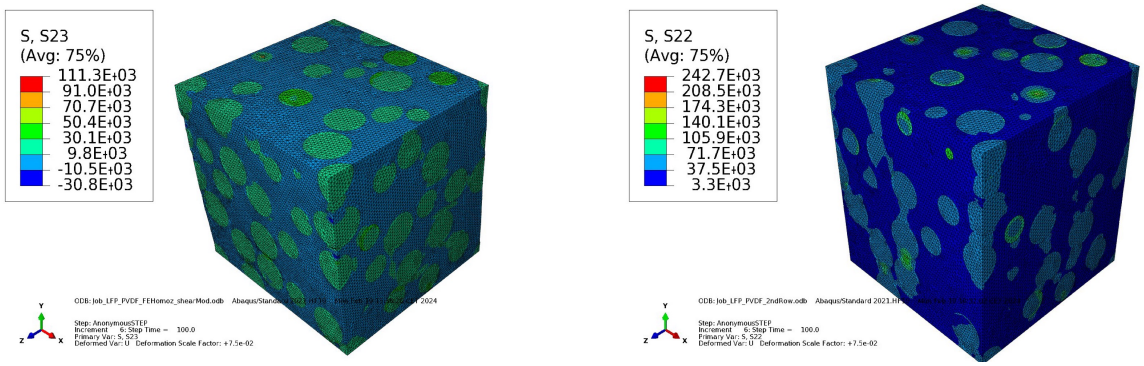

(a) **(b)**

Figure 4.1: **(a)** Stress (MPa) in 23 direction, simulated in Abaqus for extracting shear modulus, **(b)** Stress in 22 (MPa) direction, simulated in Abaqus for extracting Young's modulus in 22 direction.

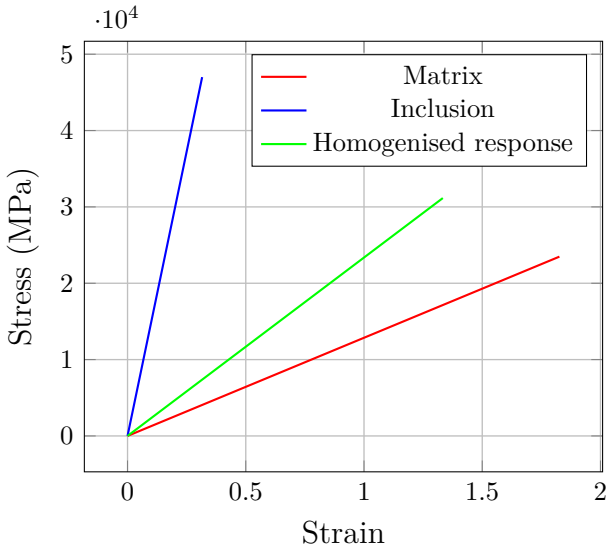

Figure 4.2: Figure to illustrate the homogenised response of the cathode.

Table 4.1: Material property of the homogenised cathode.

Electrode	**Young's modulus (GPa)**	**Shear modulus (GPa)**	**Poisson's ratio, ν (-)**
Cathode	18.71	7.46	0.26

4.1.2 Homogenised response of the anode using DBC

Similar to the cathode, the anode is also considered a linear elastic isotropic material, therefore similar load cases were also applied to this system which yields stress in 11 and 23 directions as shown in Figure 4.3.

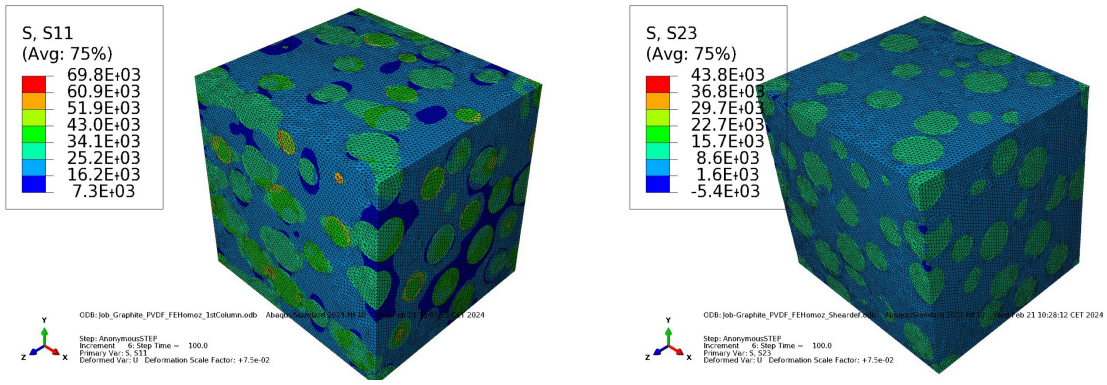

(a) **(b)**

Figure 4.3: **(a)** Stress (MPa) in 11 direction, simulated in Abaqus for extracting Young's modulus, **(b)** Stress in 23 (MPa) direction, simulated in Abaqus for extracting shear modulus in 23 direction.

The homogenisation of the anode yields the stiffness matrix represented by Equation 4.2. It clearly shows the similarity in the diagonal elements of the first 3 columns which corresponds to an isotropic material. In addition to that, even the remaining diagonal elements of the stiffness matrix are similar, which corresponds to the isotropic shear modulus of the anode. Therefore, the linear isotropic homogenised material properties of the anode can be seen in Table 4.2.

$$C_{ij} = \begin{bmatrix} 18.49 & 7.75 & 7.76 & 0 & 0 & 0 \\ 7.75 & 18.49 & 7.77 & 0 & 0 & 0 \\ 7.76 & 7.77 & 18.46 & 0 & 0 & 0 \\ 0 & 0 & 0 & 5.37 & 0 & 0 \\ 0 & 0 & 0 & 0 & 5.37 & 0 \\ 0 & 0 & 0 & 0 & 0 & 5.37 \end{bmatrix} (GPa) \tag{4.2}$$

Table 4.2: Material property of the homogenised anode.

Electrode	**Young's modulus (GPa)**	**Shear modulus (GPa)**	**Poisson's ratio, ν 0.5 cm (-)**
Anode	13.90	5.37	0.29

4.1.3 Homogenised response of the separator using DBC

The porous separator was simulated using DBCs to extract the response in the 11 and 23 directions, the stresses induced in these two cases can be seen in Figure 4.4.

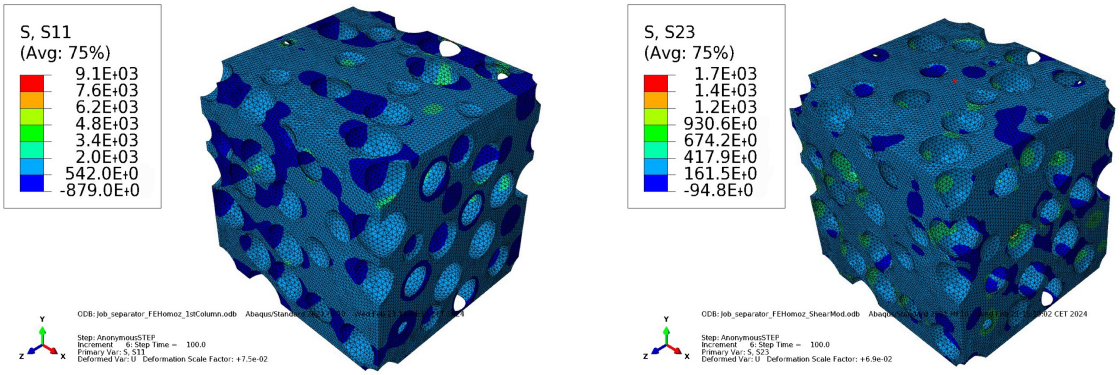

(a) **(b)**

Figure 4.4: **(a)** Stress (MPa) in 11 direction, simulated in Abaqus for extracting Young's modulus, **(b)**Stress in 23 (MPa) direction, simulated in Abaqus for extracting shear modulus in 23 direction.

The porous separator's stiffness matrix is then calculated to better understand the stress-strain relations and the coupling between them. The stiffness matrix can be seen in Equation 4.3 and the calculated modulus can be seen in Table 4.3. This demonstrates that Young's modulus and the shear modulus of the separator are very small compared to the electrodes.

$$C_{ij} = \begin{bmatrix} 0.42 & 0.15 & 0.15 & 0 & 0 & 0 \\ 0.15 & 0.42 & 0.15 & 0 & 0 & 0 \\ 0.15 & 0.15 & 0.42 & 0 & 0 & 0 \\ 0 & 0 & 0 & 0.13 & 0 & 0 \\ 0 & 0 & 0 & 0 & 0.13 & 0 \\ 0 & 0 & 0 & 0 & 0 & 0.13 \end{bmatrix} (GPa) \tag{4.3}$$

Table 4.3: Material property of the porous separator.

Battery part	**Young's modulus (GPa)**	**Shear modulus (GPa)**	**Poisson's ratio, ν (-)**
Separator	0.34	0.13	0.26

4.1.4 Homogenised response of the electrodes and the separator using PBCs

The analysis of the electrodes and separator using PBCs yields very similar results (illustrated in Table 4.4) to the DBCs. This is expected when the analysis is done in a relatively larger RVE size (40 μm in this case). As mentioned earlier, an RVE is the smallest representative volume element. The results of RVE become very consistent after a certain size, which means that a convergence study is necessary to perform at this point to find the smallest possible RVE size.

Table 4.4: Material property of the electrodes and separator using PBCs.

Electrodes/ separator	**Young's modulus, E (GPa)**	**Shear modulus, G (GPa)**	**Posson's ratio, ν (-)**
Cathode	18.21	7.16	0.27
Anode	13.36	5.17	0.29
Separator	376E-3	148E-3	0.27

4.1.5 RVE convergence study

The RVE convergence study is done to identify the smallest possible RVE size based on a volume fraction of particles of similar size, which means the size study is done to find the smallest possible RVE having the same size inclusions. In addition to that, only Young's modulus of LFP reinforced in the matrix was observed during the study. This is done because, at this stage particle/pore size, volume function and the mesh are kept constant for the cathode, anode and separator. This makes the study simple and computationally efficient. Table 4.5 demonstrates Young's modulus obtained for different RVE sizes.

Table 4.5: Material properties of the cathode using PBCs and DBCs for various RVE sizes

RVE size μm	**Young's modulus using DBC (GPa)**	**Young's modulus using PBC (GPa)**
5.3	28.03	27.41
5.5	25.72	23.9
5.8	21.42	20.29
7	21.21	18.8
10	21.17	18.12
22	18.71	18.21

4.1.6 Homogensied response of the second separator model using PBCs

The second separator model was simulated using a linear elastic material model using PBCs. The stiffness matrix of the separator is illustrated in Equation 4.4.

Table 4.6 shows that the second separator model is stiffer compared to the first separator model, which was used to develop the modelling strategy. The second separator model takes into account varied-size pores with higher volume fractions. However, separators in reality are filled with liquid electrolytes reinforced with ceramic coating materials which means that they are usually stiffer than the one modelled in this thesis.

$$C_{ij} = \begin{bmatrix} 1.4 & 0.7 & 0.7 & 0 & 0 & 0 \\ 0.7 & 1.4 & 0.7 & 0 & 0 & 0 \\ 0.7 & 0.7 & 1.4 & 0 & 0 & 0 \\ 0 & 0 & 0 & 0.3 & 0 & 0 \\ 0 & 0 & 0 & 0 & 0.3 & 0 \\ 0 & 0 & 0 & 0 & 0 & 0.3 \end{bmatrix} (GPa) \tag{4.4}$$

Table 4.6: Material property of the second separator model

Battery part	**Young's modulus (GPa)**	**Shear modulus (GPa)**	**Poisson's ratio (υ)**
Separator	0.9	0.3	0.35

4.2 Linear elastic analytical homogenisation of the material properties at the nanoscale

The analytical homogenisation gives us the upper and lower bounds of the material properties at the nanoscale. Figure 4.5 shows the Voigt and Reuss upper and lower bound for different RVE sizes. It shows that after a certain point, they remain constant throughout.

The analytical results independent of the RVE size provide upper and lower bounds of the material's response based on Voigt and Reuss assumptions. The study shows that upper and lower bounds become less sensitive to the RVE size after a certain point. The reason for this is the volume fraction of the particles obtained for different RVE sizes. Since not much volume fraction change is seen in the higher RVE size, therefore, more stability in the material's Youngs's modulus is observed.

RVE convergence study is very important to understand the material sensitivity to RVE size. Figure 4.5 illustrates the material's response to the numerical and analytical homogenisation approach based on RVE size. It is clear from the figure that an RVE size of 7 μm starts to produce repetitive results. Therefore, the study suggests that an RVE size of 7 μm is the smallest RVE which provides reasonable material properties.

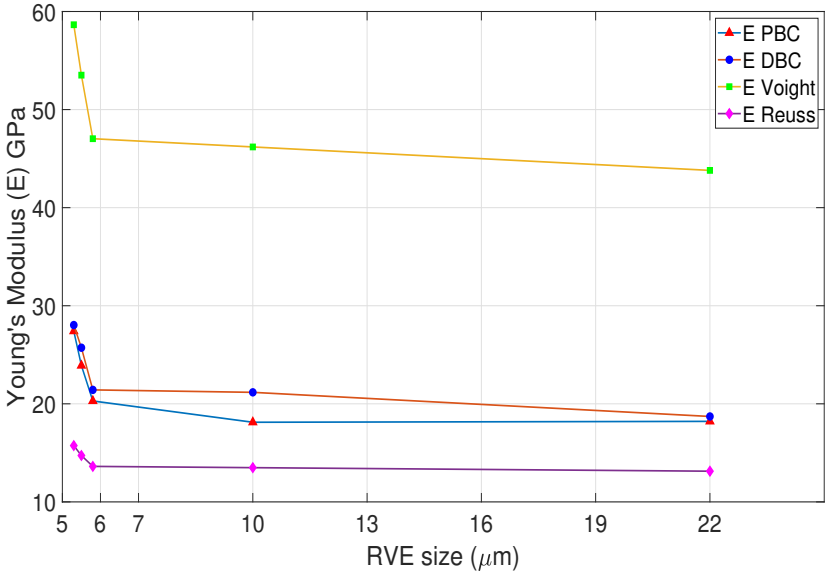

Figure 4.5: Material's response to numerical and analytical homogenisation approach based on different RVE sizes.

4.3 Hyperelastic numerical homogenisation of the material properties at nanoscale

The hyperelastic material model with an increased volume fraction of the inclusions provides insight into the response of the complex system of the matrix. The homogenised hyperelastic response of the particle-matrix system is illustrated in this section. The results provide insight into the material's dependency on battery components and their characteristics. The nature of hyperelastic material is such that they are willing to stretch, but not very willing to compress. This nature is seen in the case of the cathode and anode as well. This homogenised response of the LFP-matrix system and graphite-matrix system is then analysed to obtain the best hyperelastic model which can represent the test data. Therefore, from calibration, it is obtained that a second-order polynomial fits the best for both the cathode and anode.

4.3.1 Homogenised response of the cathode

The cathode response in both tension-compression tests yields interesting results as seen in Figures 4.6 and 4.7. Figure 4.8 demonstrates different energy potentials calibrated to obtain the response of the cathode in both tension and compression. The calibrated material parameters in Table 4.7 will further be used in the modelling of the stack.

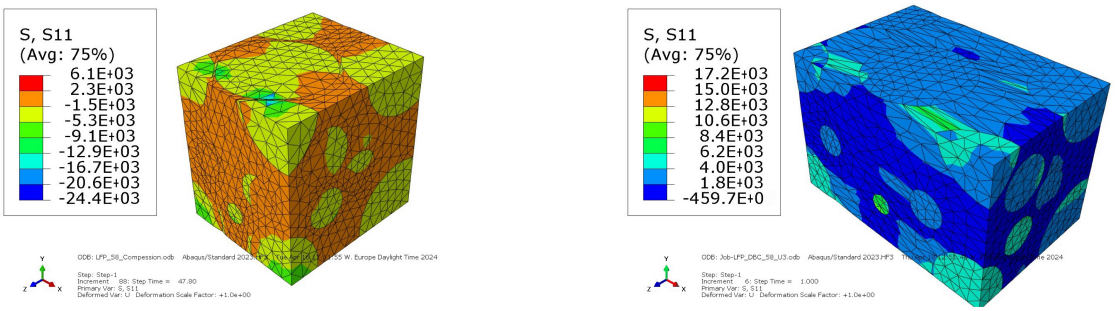

(a) **(b)**

Figure 4.6: **(a)** Compressive stress (MPa) in 11, **(b)** tensile stress (MPa) in 11 directions using a hyperelastic material model and DBCs, simulated in Abaqus for extracting the homogenised response of the particle-matrix system.

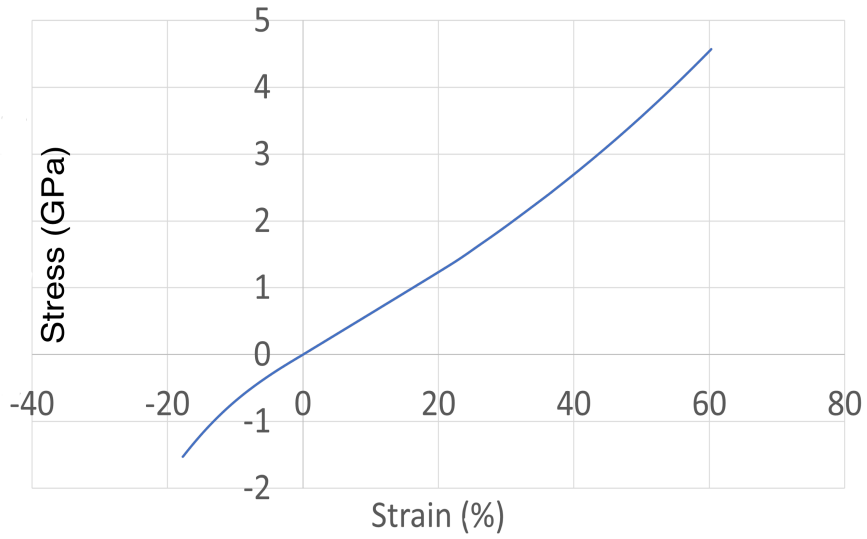

Figure 4.7: Stress vs strain graph of the homogenised response of the LFP-matrix system.

Table 4.7: Calibrated material parameters of the cathode for representing the homogenised response using second-order polynomial energy potential.

Parameters	C_{10}	C_{01}	C_{20}	C_{11}	C_{02}	D_1	D_2
Unit	GPa	GPa	GPa	GPa	GPa	GPa	GPa^{-1}
Values	1.2	-0.209	-0.73	0.227	-0.7	0	0

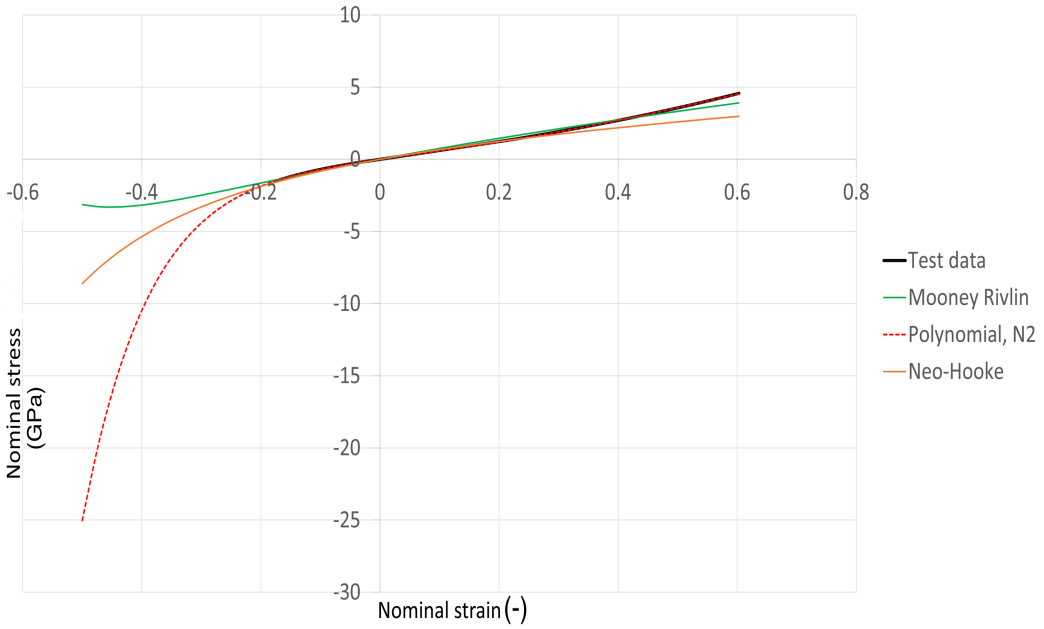

Figure 4.8: Nominal stress vs nominal strain graph for homogenised cathode response to illustrate different material model calibration with respect to the test data.

4.3.2 Homogenised response of the anode

The homogenised response of the anode for both tension and compression was extracted from the simulated results seen in Figure 4.9. Figure 4.10 illustrates the homogenised stress-strain curve. These results were used to calibrate the material parameters of the hyperelastic energy potential. The calibration was done similarly to the case of the cathode, and three energy potential functions were observed (see Figure 4.11). Table 4.8 shows the calibrated material parameter which will be used further in the modelling of the stack.

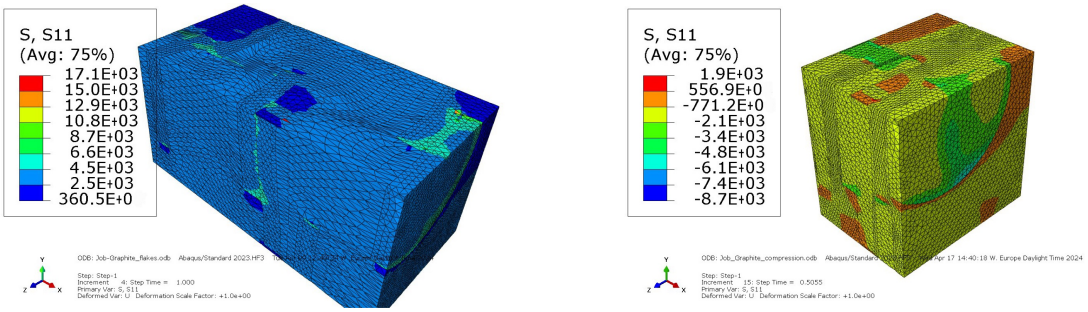

(a) **(b)**

Figure 4.9: **(a)** Tensile stress (MPa) in 11, **(b)** compressive stress (MPa) in 11 directions using hyperelastic material model implementing DBCs, simulated in Abaqus for extracting the homogenised response of the particle-matrix system.

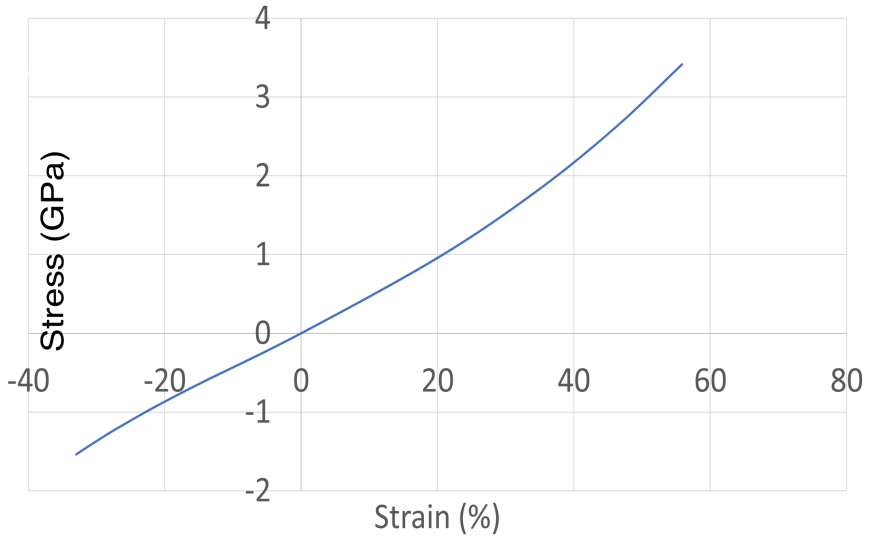

Figure 4.10: Stress vs strain graph of the homogenised response of the graphite-matrix system.

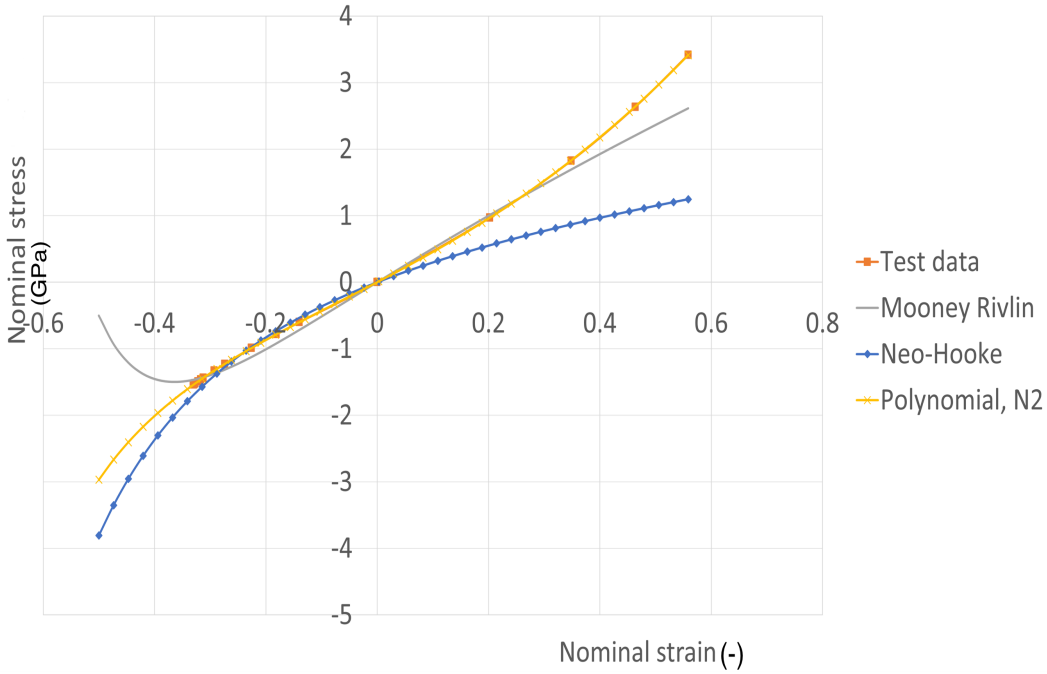

Figure 4.11: Nominal stress vs nominal strain graph for homogenised anode response to illustrate different material model calibration with respect to the test data.

Table 4.8: Calibrated material parameters of the anode for representing the homogenised response using second-order polynomial energy potential.

Parameter	C_{10}	C_{01}	C_{20}	C_{11}	C_{02}	D_1	D_2
Unit	GPa	GPa	GPa	GPa	GPa	GPa^{-1}	GPa^{-1}
Anode	1.2	-0.209	-0.73	2.27	-0.7	0	0

4.4 Linear elastic numerical and analytical homogenisation of the material properties at microscale

The linear elastic numerical homogenisation of the stack was done using a simple RVE model, this process was done to develop the modelling strategy. The response of the stack using different boundary conditions was observed and analysed. In both boundary conditions, the stack was homogenised for orthotropic material behaviour. However, it is interesting to note that the stack responds as transversely isotropic material. Further illustrative results are discussed in the proceeding subsections.

4.4.1 Homogenised response of the stack using DBC

The stack RVE with DBCs was simulated using Abaqus. The main goal was to extract the homogenised 6X6 stiffness matrix, hence, all 6 load cases were analysed during the process. Figure 4.12 illustrates 2 load cases out of the 6, of which Figure 4.12(a) shows the induced stress in 11 directions, which was done to extract the C_{11}. Figure 4.12 (b) shows the induced shear stress in 23 directions which was done to extract C_{66}. Equation 4.5 and Table 4.9 shows the complete stiffness matrix and the respective material properties of the stack.

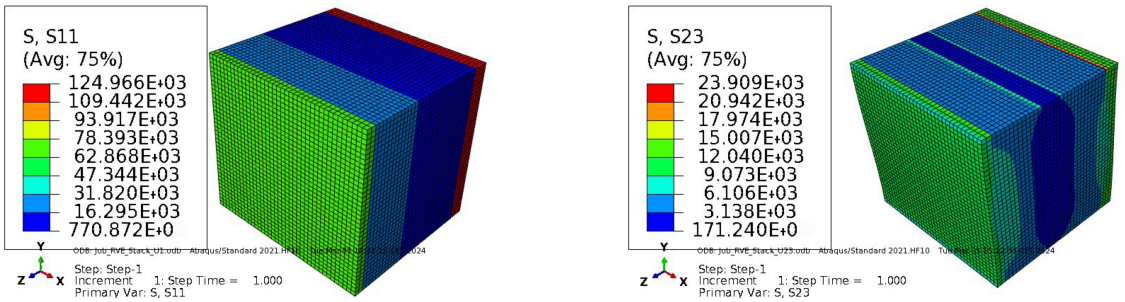

(a) **(b)**

Figure 4.12: **(a)** Stress (MPa) in 11, **(b)** tensile stress (MPa) in 23 directions using DBCs, simulated in Abaqus for extracting the homogenised response of the stack.

$$C_{ij} = \begin{bmatrix} 30.7 & 9.8 & 1.1 & 0 & 0 & 0 \\ 9.8 & 30.7 & 1.1 & 0 & 0 & 0 \\ 1.1 & 1.1 & 2.8 & 0 & 0 & 0 \\ 0 & 0 & 0 & 10.42 & 0 & 0 \\ 0 & 0 & 0 & 0 & 4.7 & 0 \\ 0 & 0 & 0 & 0 & 0 & 4.7 \end{bmatrix} (GPa) \tag{4.5}$$

Table 4.9: Material properties of the stack using DBC

Unit (GPa)	E1	E2	E3	G23	G12	G13
Stack	24.6	24.6	2.74	4.7	10.4	4.7

4.4.2 Homogenised response of the stack using PBC

The stack was simulated in two different solvers using PBC. Both cases reveal similar results. However, the analysis consists of all the 6 load cases being simulated. Table 4.10 and Equation 4.6 illustrate the material properties and the respective stiffness matrix of the stack.

Table 4.10: Material properties of the stack using PBC

Unit (GPa)	E1	E2	E3	G23	G12	G13
Stack	25.4	25.4	2.7	0.9	9.7	0.9

$$C_{ij} = \begin{bmatrix} 28.54 & 9.8 & 1.1 & 0 & 0 & 0 \\ 9.8 & 30.75 & 1.1 & 0 & 0 & 0 \\ 1.1 & 1.1 & 2.9 & 0 & 0 & 0 \\ 0 & 0 & 0 & 9.7 & 0 & 0 \\ 0 & 0 & 0 & 0 & 0.9 & 0 \\ 0 & 0 & 0 & 0 & 0 & 0.9 \end{bmatrix} (GPa) \tag{4.6}$$

It is seen from the results that the developed stress is maximum at the current collector in both tension and shear, and there is stress concentration near the separator. The reason for such behaviour is because of the stiffer material properties of the metals compared to cathode and anode, when it comes to the separator, as discussed earlier, it is very soft, since the separator modelled in this study does not take into account the reinforcement, which is usually seen in the commercial separators.

Similar to nanoscale a comparative analysis was done for the stack too. To assess the accuracy of the results both Voigt and Reuss upper and lower bounds were also checked. Figure 4.13 demonstrates that the results from both the solver in the case of PBCs and DBCs are well within the limits of the upper and lower bound. Therefore, this ensures the reliability of the model being developed. Given the accuracy of the linear elastic model, now further advanced material models like hyperelastic and crushable foam can be implemented.

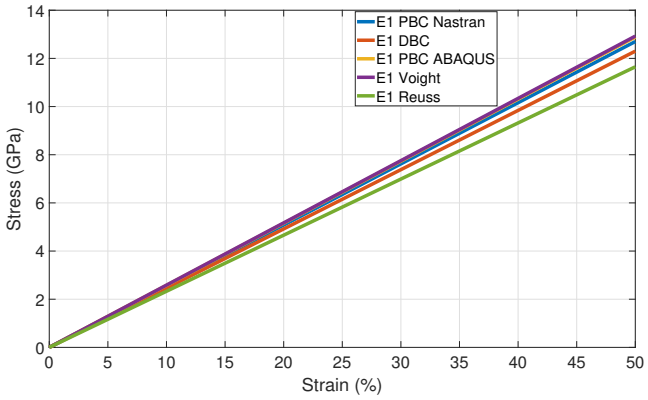

Figure 4.13: Material's response to numerical and analytical homogenisation approaches using different solvers and boundary conditions.

4.5 Hyperelastic numerical homogenisation of the material properties at microscale

The hyperelastic homogenised material response of the stack is demonstrated in Figure 4.14, illustrating the induced stress and strain in 33 directions throughout the layers. Figure 4.15 illustrates the stack's non-linear homogenised stress vs strain response. The material calibration was done to obtain the best energy potential which will be used to model the final jellyroll model. Figure 4.16 illustrates the stress vs strain graph of different energy potentials.

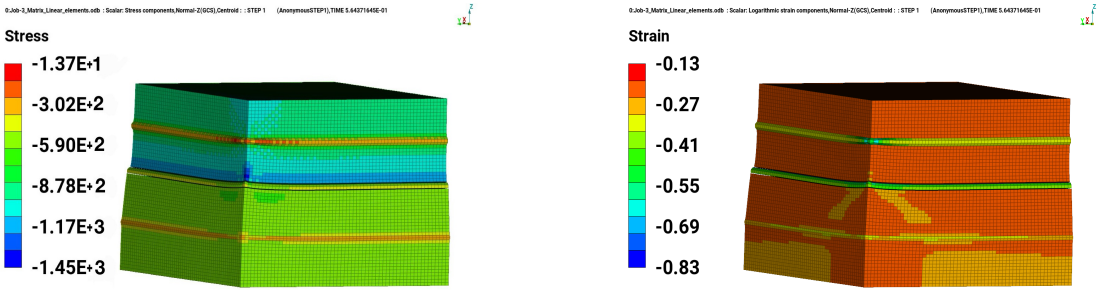

(a) **(b)**

Figure 4.14: **(a)** Compressive stress (MPa) in 33, **(b)** Compressive strain in 33 directions using hyperelastic material model implementing DBCs, simulated in Abaqus for extracting the homogenised response of the stack.

Implementation of the hyperelastic material model for the stack shows that it is difficult for such material to be compressed and therefore to obtain a compressive strain of 27%, approximately 500 MPa of stress is developed. It is also important to note that during the compression, higher stress is developed at the electrodes, however, higher strain is seen in the current collector. This shows the hyperelastic

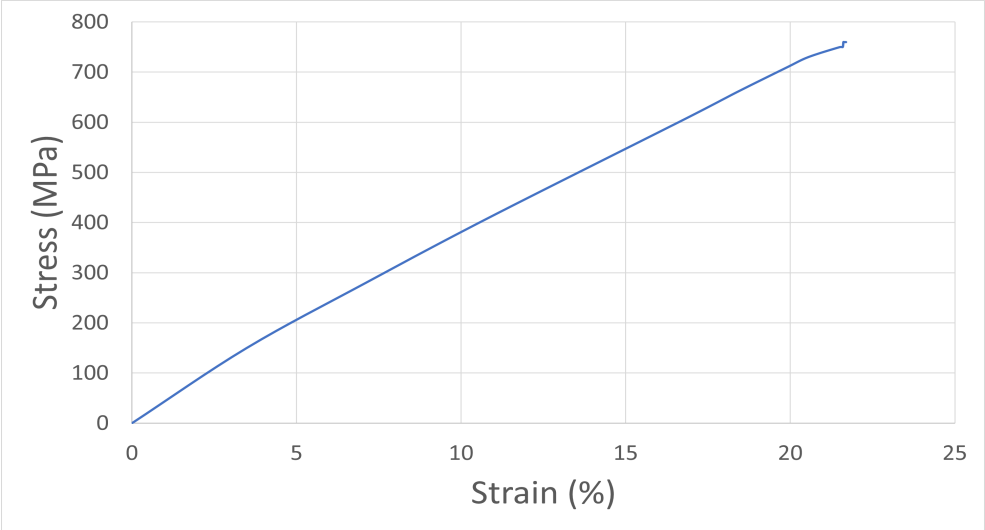

Figure 4.15: Stress vs strain relation as a homogenised stack response under compression in 33 direction.

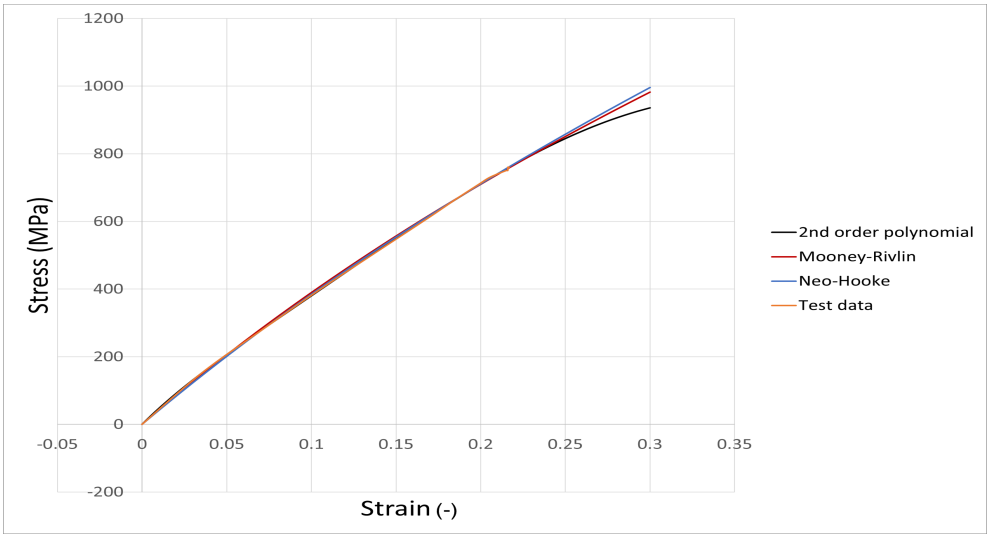

Figure 4.16: Different energy potential calibrated to observe the best fit for the obtained homogenised response of the stack.

nature of the electrode coating. The stress-strain diagram in Figure 4.15 shows a non-linear response, but the material overall shows a stiff response in the z-direction.

The material calibration of different energy potentials, to show the homogenised response of the stack yields similar results for the three cases. However, the second-order polynomial will be used for the modelling of the jellyroll because of fact that it has 7 parameters to control the curve which makes it more stable at higher strains.

4.6 Crushable foam numerical homogenisation of the material properties at microscale

The crushable foam material response of the stack is illustrated in Figure 4.17, in the form of induced stress and strain in 33 direction throughout the layers. Figure 4.18 shows the linear elastic and volumetric hardening nature of the stack. The plastic stress and strain data from this response is used as the input load curve in the full-scale modelling of the jellyroll.

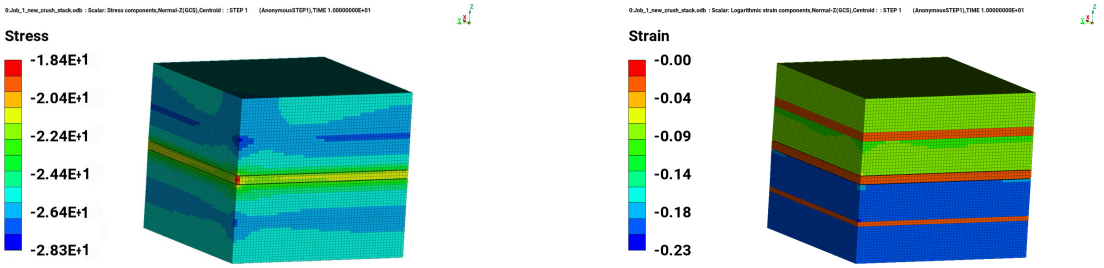

(a) **(b)**

Figure 4.17: **(a)** Compressive stress (MPa) in 33, **(b)** Compressive strain in 33 directions using crushable foam material model implementing DBCs, simulated in Abaqus for extracting the homogenised response of the stack.

The results from the stress response from Figure 4.17 illustrate that the stress levels are relatively low compared to the hyperelastic model. In the hyperelastic model, higher stresses are observed in the electrode layer, despite having lower strain levels. It is quite the opposite in the crushable foam model. The current collectors have negligible amounts of strains compared with the hyperelastic model. This is one of the advantages of the crushable foam material model. As explained earlier, the role of metallic current collectors is not prominent in compression. Therefore, in the crushable foam model, more realistic behaviour is observed, whereas in the hyperelastic model, the current collectors were getting strained significantly and their corresponding stress levels were high. Therefore, it is assumed that the crushable foam material model provides a more realistic representation of the stack behaviour.

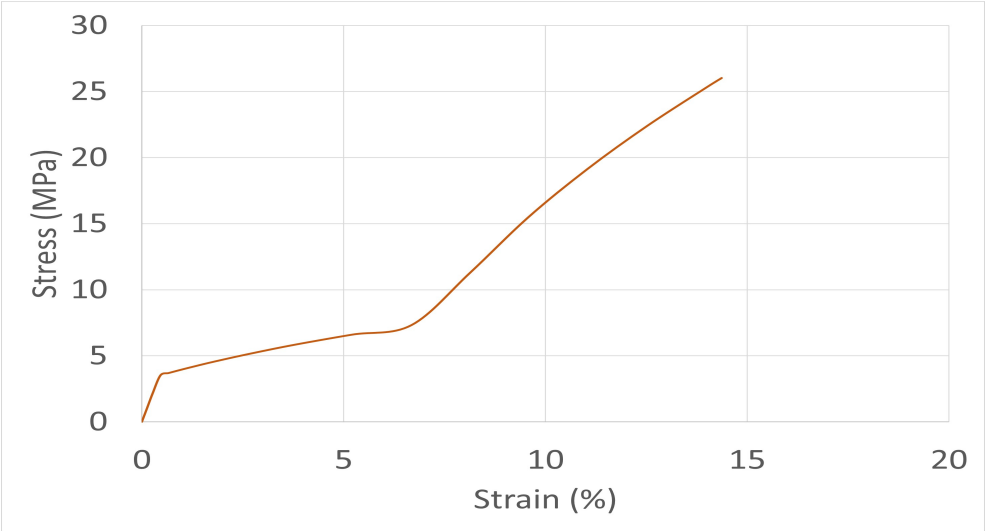

Figure 4.18: Crushable foam material stress-strain plot of the homogenised response of the stack under compressive loading.

4.7 Full-scale hyperelastic jellyroll modelling

The full-scale jellyroll model provides insight into the material model being developed so far. Since this is the final step of the modelling strategy, it provides comparative results with the test data. Figure 4.19 demonstrates the stress and strains induced in the jellyroll during an impact loading using a second-order hyperelastic material model. Figure 4.20 illustrates that the hyperelastic model response is much stiffer than the actual test data. This reveals that hyperelastic modelling is less accurate for predicting the mechanical response of complex material system.

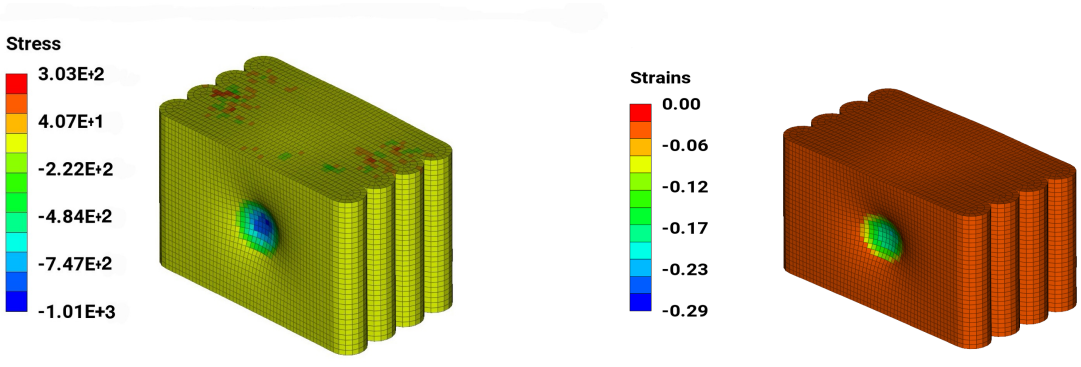

(a) **(b)**

Figure 4.19: **(a)** Compressive stress (MPa) in 11, **(b)** Compressive strain in 11 directions in the jellyroll using the hyperelastic material model.

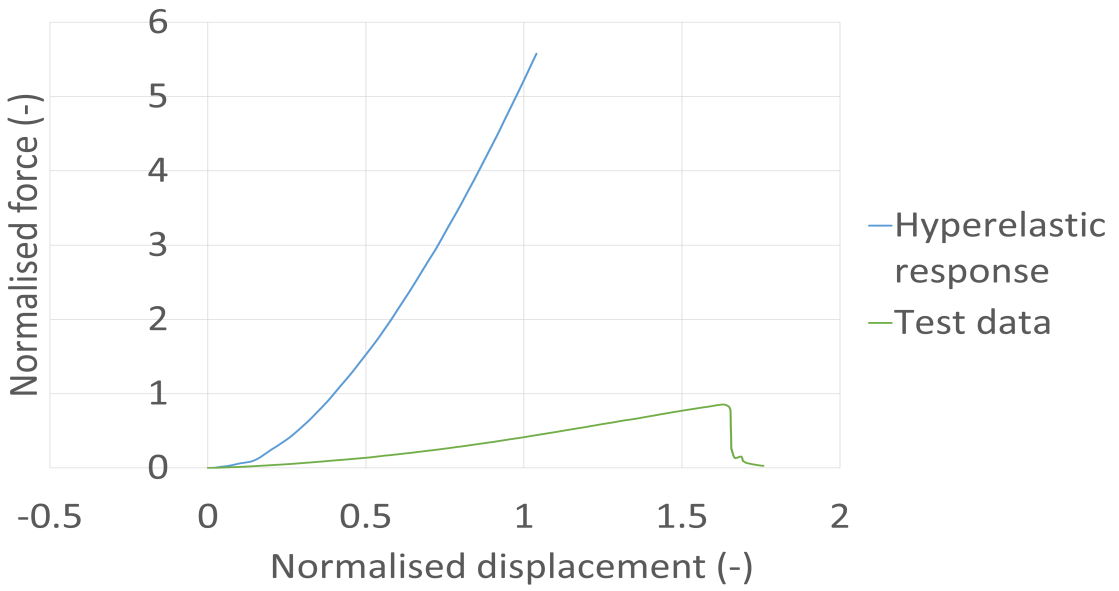

Figure 4.20: Comparative analysis of the force vs displacement obtained from the simulation of jellyroll with cell casing (as seen in Figure 3.6) using the hyperelastic material model and the test data.

4.8 Full-scale crushable foam jellyroll modelling

The homogenised response of the crushable foam stack RVE is implemented into the jellyroll and then simulated to validate the test results. The simulation yields the jellyroll response in the form of stress and strain as shown in Figure 4.21. The overall force vs displacement curve is obtained for it and then compared with the existing test data. Figure 4.22 illustrates the comparison of both curves.

Figure 4.22 show that the simulated result of the crushable foam jellyroll model starts to exhibit volumetric hardening at an early phase. This is because elasticity is very small, corresponding to almost negligible strain level for yielding. Therefore, the material goes into plasticity quite early.

The crushable foam jellyroll model shows promising results. The response is softer than the real test data, which shows that with proper material data, it is possible to obtain a similar response to the test data. The battery chemistry of the tested cell is NMC, however, the available material properties used in this thesis are of LPF chemistry. Therefore, the crushable foam material model is considered as more appropriate approach to move ahead in this field.

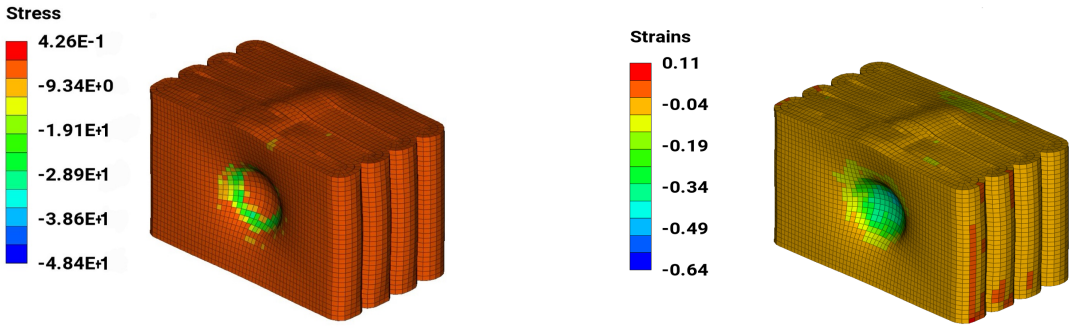

(a) (b)

Figure 4.21: **(a)** Compressive stress (MPa) in 11, **(b)** Compressive strain in 11 directions in the jellyroll using the crushable foam material model.

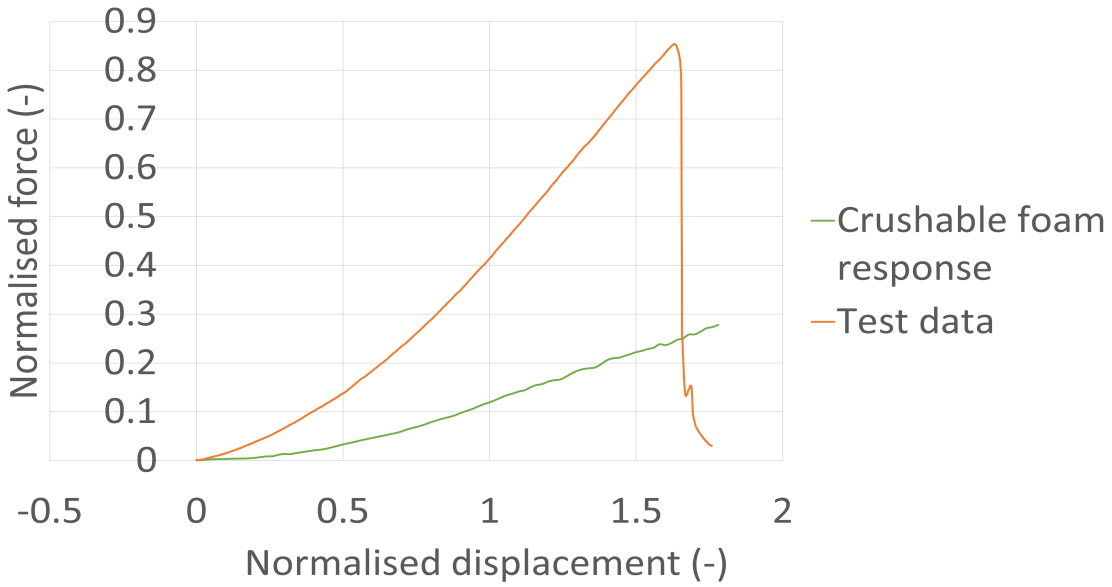

Figure 4.22: Force vs displacement curve of the jellyroll with cell casing simulated using crushable foam material model.

5
Conclusion

The study was carried out to develop a virtual testing strategy for the Li-ion batteries under mechanical loads. The study thoroughly examined different material models; linear elastic, hyper-elastic and crushable foam. The linear elastic modelling was a preliminary approach to establish the methodology. The complex matrix system of the electrodes comes with a non-linear stress-strain relationship. Therefore, hyperelastic modelling was the very first approach to address this complexity. The homogenisation was done at different scales; nanoscale, microscale and the final validation at the full-scale jellyroll model.

This study reveals that hyperelastic modelling is not an appropriate approach. The batteries which are more prone to compressive loads, exhibit very stiff responses with hyperelastic modelling. Moreover, the material properties required to do hyperelastic modelling are very rigorous. It is difficult to obtain the particles and the PVDF-CB-electrolyte matrix system properties. Furthermore, crushable foam material modelling was done at the intermediate stage, which is modelling the RVE at the microscale. This approach with data from literature sources revealed that in reality, electrodes exhibit yielding after a certain strain level. In addition to that, it was also observed that electrodes undergo volumetric hardening during compressive loads. The validation stage, which is modelling the jellyroll and comparison with the test data shows that crushable foam modelling is softer than the test data. This illustrates that with proper material properties, and calibration of the model, it is potentially possible to develop a reliable material model for the battery.

With this modelling strategy, it is possible to scale up the stress and strains between the jellyroll and the stack. This allows to understand the state of stress and strains in the individual components; electrodes and separators. Therefore, a failure surface can be created linked to the appropriate failure modes to better understand the short-circuit phenomena under mechanical loading scenarios in the batteries. This concept is similar to e.g., the concept of first-ply failure in composite materials.

6
Future Work

6.1 Component testing for material properties

This thesis aimed to develop a virtual testing methodology implementing different material models. The data used are purely from the literature resources and are not similar to the test data which is used for comparative analysis. Therefore, to accurately predict the material's response to mechanical load, it is important to obtain data necessary for the material modelling. The results revealed that microscale modelling is the right approach to begin with, rather than the nanoscale. Hence, certain tests are to be done at the stack level.

For component testing, the cells should be discharged to 0% SOC. The samples are to be cut from the jellyroll for uniaxial tensile, compression and biaxial tensile tests.

6.1.1 Uniaxial tensile test

Samples of anode, cathode, and separator are to be cut from the jellyrolls with a width of 10 mm for uniaxial tensile tests [1]. Since the separator exhibits in-plane anisotropy, hence, two sets of samples, one in MD and the other in TD are to be cut for the separator [1]. The strain rate should be 2mm/min for the electrode and 4mm/min for the separator. A load capacity of 100 N monotonic loading machine should be used.

6.1.2 Uniaxial compression test

The test should be conducted on round samples of approximately 16 mm in diameter. All the experiments are to be carried out at a 1mm/min strain rate [1]. During compression tests, it is very important to observe the behaviour of the material fracture. It provides insight into the material model to be used and the fracture mechanics associated with it.

6.1.3 Biaxial tensile test

Uniaxial tensile tests are prone to higher error. This is mainly because of the damage to the edges of the samples during sample preparation. This leads to premature failure of the specimen. Another factor is the nonuniform pressure of the grips holding the specimen. Therefore, to eliminate these errors it is important to perform the biaxial tensile test on the samples. The test can be carried out using a 1/2 inch

punch at a speed of 12 mm/min [1]. The load-displacement curve is to be noted, and the failure modes are to be observed during the process.

6.2 Time dependent effects on battery

In this thesis, time-dependent effects on the battery are considered as limitations. However, it is very important to incorporate these effects in the material model. The battery shows different chemical and material characteristics based on the state of charge (SOC) and state of health (SOH) which results in swelling and changes in the elastic properties of the constituents.

6.2.1 Effect of state of charge

The effect of SOC on the battery is significant when considering the battery as a material. When SOC is zero which corresponds to the fully discharged battery, the cathode is in the form of LFP and the anode is in the form of graphite (C). When the SOC is 1 which corresponds to the fully charged battery, the cathode is in the form of $FeP0_4$ and the anode is in the form of LiC_6. Therefore, based on the SOC two different compounds serve the respective electrodes; cathode and anode. These two different compounds have different material properties; Young's modulus (E), Shear Modulus (G) and Poisson's ratio (υ) [17]. In the case of the cathode, the change is not significant, however, in the case of the anode it is a significant change in the elastic modulus as seen in Figure 6.1.

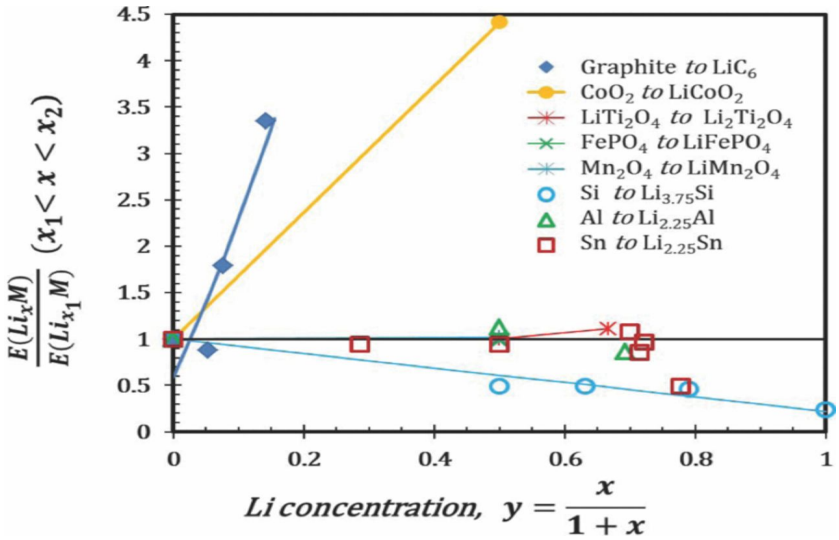

Figure 6.1: Figure demonstrating the change in material property (Young's Modulus) when normalised Li concentration goes from 0 to 1. It shows that for the LFP the normalised average Young's modulus is close to 1 when Li concentration goes from 0 to 1, whereas for graphite, the normalised average Young's modulus increases significantly when Li concentration goes from 0 to 1. Reprint from [17]

.

6.2.2 Effect of swelling

When charged and discharged, the battery undergoes breathing. In other words, when the battery is fully charged it expands and when it is discharged it shrinks back due to several factors, e.g., intercalation and de-intercalation process of lithium [21]-[22]. However, this process is not fully reversible, therefore, with time this small irreversibility leads to a permanent change in the size of the battery. The effect of swelling is not just mechanical, but electrochemical as well. It corresponds to the SOH of the battery, i.e., as the battery swells the performance and the efficiency decreases. During charging, Li-ions travel from the cathode to the anode through the electrolyte. As shown in Figure 6.2 cathode material typically shows reduced volume during the charging stage while the anode exhibits positive volumetric strain [21]. However, the reduction in volume at the cathode is not equal to the volumetric expansion of the anode material.

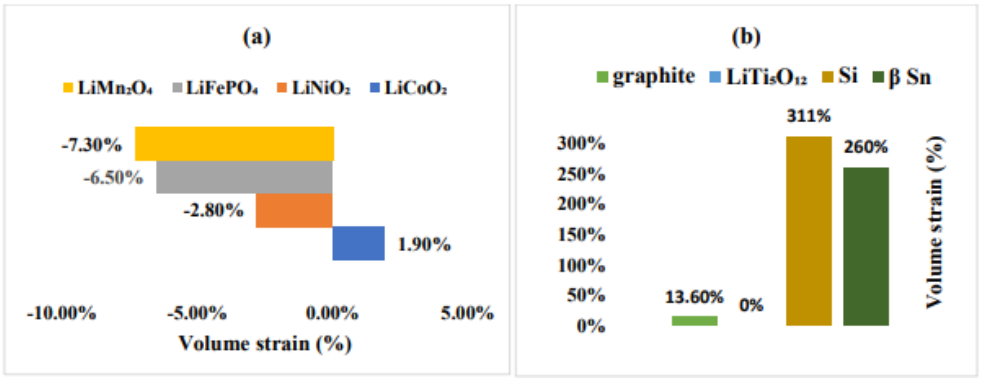

Figure 6.2: Volumetric strain in the cathode (a) and anode (b) corresponding to different battery chemistry due to intercalation and de-intercalation of Li-ion. Reprint from [21].

Therefore, a methodology study has to be carried out to implement these effects in the material model. This will make the model very robust and close to reality. The mentioned references in this section are to be studied and a thorough analysis is to be carried out. The approach to address the cell swelling can be implementing the swelling effect as a residual stress. The same can be done using multiple-step modelling in Abaqus. Therefore, Step 1 will implement the residual stress by implementing an effective thermal expansion coefficient load case. Step 2 subsequently implements the mechanical load case.

Figure 6.1 shows that the SOC dependency of the material stiffness modulus is linear. Therefore interpolation of the material properties can be done for different SOC levels and similarly can be implemented in the modelling. However, these strategies are potential modelling ideas, but might not be the exact right approach. Therefore, the reader can brainstorm these ideas and develop the methodology based on further literature studies.

Bibliography

[1] E. Sahraei, M. M. Keshavarzi, X. Zhang, and B. Lai, "Mechanical Properties of Prismatic Li-Ion Batteries—Electrodes, Cells, and Stacks," *Journal of Electrochemical Energy Conversion and Storage*, vol. 19, no. 4, May 2022, ISSN: 23816910. DOI: 10.1115/1.4054823.

[2] D. Clerici, F. Mocera, and A. Somà, "Experimental characterization of lithium-ion cell strain using laser sensors," *Energies*, vol. 14, no. 19, Oct. 2021, ISSN: 19961073. DOI: 10.3390/en14196281.

[3] L. Greve and C. Fehrenbach, "Mechanical testing and macro-mechanical finite element simulation of the deformation, fracture, and short circuit initiation of cylindrical Lithium ion battery cells," *Journal of Power Sources*, vol. 214, pp. 377–385, May 2012, ISSN: 03787753. DOI: 10.1016/j.jpowsour.2012.04.055.

[4] J. Xu, B. Liu, X. Wang, and D. Hu, "Computational model of 18650 lithium-ion battery with coupled strain rate and SOC dependencies," *Applied Energy*, vol. 172, pp. 180–189, May 2016, ISSN: 03062619. DOI: 10.1016/j.apenergy.2016.03.108.

[5] P. Gupta and P. Gudmundson, "Modeling of local electrode stresses and pressures in lithium-ion battery packs using three-dimensional homogenization," *Journal of Power Sources*, vol. 582, May 2023, ISSN: 03787753. DOI: 10.1016/j.jpowsour.2023.233514.

[6] *Volvo EX90 specifications*. [Online]. Available: https://www.volvocars.com/uk/cars/ex90-electric/specifications/.

[7] X. Lu, A. Bertei, D. P. Finegan, *et al.*, "3D microstructure design of lithium-ion battery electrodes assisted by X-ray nano-computed tomography and modelling," *Nature Communications*, vol. 11, no. 1, May 2020, ISSN: 20411723. DOI: 10.1038/s41467-020-15811-x.

[8] *Battery Atlas 2022*, 2022. [Online]. Available: https://www.pem.rwth-aachen.de/global/show_document.asp?id=aaaaaaaabpjuwfj.

[9] P. U. Nzereogu, A. D. Omah, F. I. Ezema, E. I. Iwuoha, and A. C. Nwanya, "Anode materials for lithium-ion batteries: A review," *Applied Surface Science Advances*, vol. 9, Jun. 2022, ISSN: 26665239. DOI: 10.1016/j.apsadv.2022.100233.

[10] K. Runesson and R. Larsson, *Constitutive modeling of engineering materials-theory and computation*, The Primer. Göteborg.: Department of Industrial and Materials Science, Chalmers University of Technology.

[11] *Challenges and solutions in battery safety*, 2023. [Online]. Available: https://www.pem.rwth-aachen.de/global/show_document.asp?id=aaaaaaaacclpluf.

[12] E. J. Barbero, *Finite element analysis of composite materials using Abaqus*. CRC Press, May 2023, ISBN: 9781466516618. DOI: https://doi.org/10.1201/9781003108153.

[13] Javier Bonet, Antonio J. Gil, and Richard D. Wood, *Nonlinear Solid Mechanics for Finite Element Analysis: Statics*. Cambridge University Press, Jun. 2016, pp. 158–187. DOI: https://doi.org/10.1017/CBO9781316336144.007.

[14] M. Smith, *ABAQUS/Standard User's Manual, Version 6.9*. Dassault Systèmes Simulia Corp, 2009.

[15] L. J. Gibson and M. F. Ashby, *The mechanics of foams: basic results*. Cambridge University Press, May 2014, pp. 175–234. DOI: 10.1017/cbo9781139878326.007.

[16] S. K. Michael Okereke, *Finite Element Applications*. 2018, ISBN: 978-3-319-67125-3. DOI: https://doi.org/10.1007/978-3-319-67125-3.

[17] Y. Qi, L. G. Hector, C. James, and K. J. Kim, "Lithium Concentration Dependent Elastic Properties of Battery Electrode Materials from First Principles Calculations," *Journal of The Electrochemical Society*, vol. 161, no. 11, F3010–F3018, 2014, ISSN: 0013-4651. DOI: 10.1149/2.0031411jes.

[18] A. H. S. Iyer, P. Gupta, P. Gudmundson, and A. Kulachenko, "Measuring microscale mechanical properties of PVdF binder phase and the binder-particle interface using micromechanical testing," *Materials Science and Engineering: A*, vol. 881, May 2023, ISSN: 09215093. DOI: 10.1016/j.msea.2023.145352.

[19] G. K. Elyashevich, I. S. Kuryndin, and E. Y. Rosova, "Composite membranes with conducting polymer microtubules as new electroactive and transport systems," *Polymers for Advanced Technologies*, vol. 13, no. 10-12, pp. 725–736, 2002, ISSN: 10427147. DOI: 10.1002/pat.251.

[20] *Matweb*. [Online]. Available: https://www.matweb.com/index.aspx.

[21] K. Kalaikkanal, N. Gobinath, and R. Mohan, "Influence of swelling on the safety aspects of electric vehicle batteries - Short Review," in *IOP Conference Series: Earth and Environmental Science*, vol. 1161, Institute of Physics, 2023. DOI: 10.1088/1755-1315/1161/1/012010.

[22] A. Knutsson and J. Trombati, "Finite Element Modelling of Cell Swelling for Traction Batteries," *Chalmers University of Technology, Göteborg*, 2021. [Online]. Available: https://hdl.handle.net/20.500.12380/302381.

A

Appendix 1

Abaqus input file example

```
1  *Heading
2  ** Constraint: T1;CONSTRAINT-1-1-1-1-1-1-1-1-1-1-1
3  *Tie, name=T1;CONSTRAINT-1-1-1-1-1-1-1-1-1-1-1, adjust=no, ...
       position tolerance=1., type=SURFACE TO SURFACE
4  S30;_PICKEDSURF29, S29;_PICKEDSURF28
5  ** Constraint: T2;CONSTRAINT-2-1-1-1-1-1-1-1-1-1-1
6  *Tie, name=T2;CONSTRAINT-2-1-1-1-1-1-1-1-1-1-1, adjust=no, ...
       position tolerance=1., type=SURFACE TO SURFACE
7  S28;_PICKEDSURF27, S27;_PICKEDSURF26
8  *End Assembly
9  **
10 ** MATERIALS hyperelastic model
11 **
12 **         M1;CATHODE
13 **
14 *Material, name=ANODE
15 *Density
16  7.85e-09,
17 *Hyperelastic, n=2, test data input
18 *Uniaxial Test Data
19  -0.000600258, -0.139725
20             0.,        0.
21   0.000968735,  0.202143
22
23 **       Cathode_updated
24 **
25 *Material, name=CATHODE_UPDATED
26 *Density
27  7.85e-09,
28 *Hyperelastic, n=2, test data input
29 *Uniaxial Test Data
30  -2.05148e-05, -0.00341312
31             0.,          0.
32    0.00133103,    0.215541
33
34 **         M17;CU_CC
35 **
36 *Material, name=M17;CU_CC
37 *Density
38  7.85e-09,
```

```
*Elastic
 0.11, 0.3
*Plastic
 3.3e-05,  0.
 0.00021, 0.2
**         M20;AL_CC
**
*Material, name=M20;AL_CC
*Density
 7.85e-09,
*Elastic
 0.068, 0.36
*Plastic
 0.000276,   0.
  0.00031, 0.15
**         M16;SEPARATOR
**
*Material, name=SEPARATOR
*Density
 7.85e-09,
*Elastic
 0.000999, 0.35
** ----------------------------------------------------------------
**
** STEP: AnonymousSTEP1
**
*Step, name=AnonymousSTEP1, nlgeom=YES
*Static
0.1, 1., 1e-05, 1.
**
** BOUNDARY CONDITIONS
**
** Name: Disp-BC-1 Type: Displacement/Rotation
*Boundary
_PICKEDSET50, 3, 3, -100.
** Name: Disp-BC-2 Type: Symmetry/Antisymmetry/Encastre
*Boundary
_PICKEDSET51, XSYMM
** Name: Disp-BC-3 Type: Symmetry/Antisymmetry/Encastre
*Boundary
SET-35, YSYMM
** Name: Disp-BC-6 Type: Symmetry/Antisymmetry/Encastre
*Boundary
SET-38, ZSYMM
**
** OUTPUT REQUESTS
*End Step
```

DEPARTMENT OF INDUSTRIAL and MATERIALS SCIENCE
CHALMERS UNIVERSITY OF TECHNOLOGY
Gothenburg, Sweden
www.chalmers.se

CHALMERS
UNIVERSITY OF TECHNOLOGY